State-resolved modeling of electronic excitation in weakly ionized oxygen mixtures

Timothy T. Aiken [*] and Iain D. Boyd [†]

Ann and H. J. Smead Department of Aerospace Engineering Sciences, University of Colorado, Boulder, Colorado 80309, USA

(Received 1 October 2023; accepted 5 March 2024; published 8 April 2024)

Electronic excitation and ionization in oxygen-argon mixtures are analyzed using a three-temperature electronic state-resolved model and evaluated using recent experimental data from reflected shock experiments. A detailed description of the model formulation and parameter selection is provided. Excellent agreement is obtained between model predictions and experimental measurements of O_2 number density during dissociation in mixtures of 2%–5% O_2 dilute in argon. Next, electron number density measurements are leveraged to infer a rate constant for the heavy particle impact excitation of argon, facilitating improved modeling of net ionization and a clearer understanding of the electronic excitation kinetics of oxygen. The electronic state-resolved model is then assessed using measured data for three electronic states of atomic oxygen. The model successfully reproduces the multistage behavior observed in the measured time histories and yields new insights into the multistage behavior that revises previous interpretations. For several experiments, the modeling choices involved in the calculation of escape factors significantly influence the predicted time histories. A global sensitivity analysis considering nearly 300 parameters is then conducted to identify which model parameters most sensitively influence the predicted excited state populations. Excitation of the measured states from the metastable levels and collisional excitation between the three measured states are important across all conditions. The excited state populations demonstrate complex sensitivities involving a large number of collisional and radiative processes, highlighting the importance of adopting a detailed modeling approach when interpreting excited state measurements.

DOI: 10.1103/PhysRevE.109.045203

I. INTRODUCTION

During atmospheric reentry, a strong bow shock is formed in front of the spacecraft that compresses and heats the freestream flow, initiating complex physicochemical processes in the gas surrounding the vehicle. A key complexity of these hypersonic flows is that the timescales of internal mode excitation, chemical reactions, and flow advection are all similar, meaning that the flow is in a thermochemical nonequilibrium state. Accurate modeling of this nonequilibrium behavior is required for predictions of radiative [1] and convective [2] heat flux, radio communications blackout [3], and vehicle radiative signatures [4].

Nonequilibrium thermochemistry is most commonly modeled in vehicle-scale computational fluid dynamic (CFD) calculations using a multitemperature model [5]. This type of model is based on the framework of mode approximation, where separate energy conservation equations are solved to account for nonequilibrium between different energy modes of the gas. Within the mode approximation, the distribution of particle internal energies—rotational, vibrational, electronic—is assumed to follow Boltzmann statistics. However, the true energy distribution function is generally non-Boltzmann, and this distinction affects the rates of dissociation, ionization, and thermal relaxation, which, in turn, affect engineering quantities of interest like heating.

State-resolved modeling provides a more accurate alternative to multitemperature models by removing the assumption of a Boltzmann distribution and directly resolving the populations of individual internal energy levels. Significant advancements in the understanding of molecular vibrational relaxation and dissociation have been enabled by state-resolved models that use rate coefficients determined from scattering calculations on *ab initio* potential energy surfaces [6]. State-resolved modeling of electronic excitation and ionization is comparatively less mature since it is far more difficult to determine the necessary rate coefficients using *ab initio* techniques, particularly for collisions involving two heavy particles. As a result, experimental measurements play an essential role in not only the validation of electronic state-resolved models but also their development.

The nonequilibrium electronic excitation of atomic oxygen is of particular interest since atomic radiation is a major contributor to vehicle heating during high-speed Earth entry. In addition, it has recently been shown that all of the dominant associative ionization reactions in hypersonic air flows occur primarily through the interaction of electronically excited atoms [7]. Thus, atomic electronic excitation is an essential precursor to the formation of free electrons behind strong shock waves in air.

The current study is motivated by recent measurements of electronically excited oxygen atoms in shock tube experiments [8–11] that provide a unique and valuable opportunity to study the excitation and ionization kinetics of highly excited oxygen atoms. The experiments have previously been studied using simplified electronic state-resolved mod-

[*] timothy.aiken@colorado.edu
[†] iain.boyd@colorado.edu

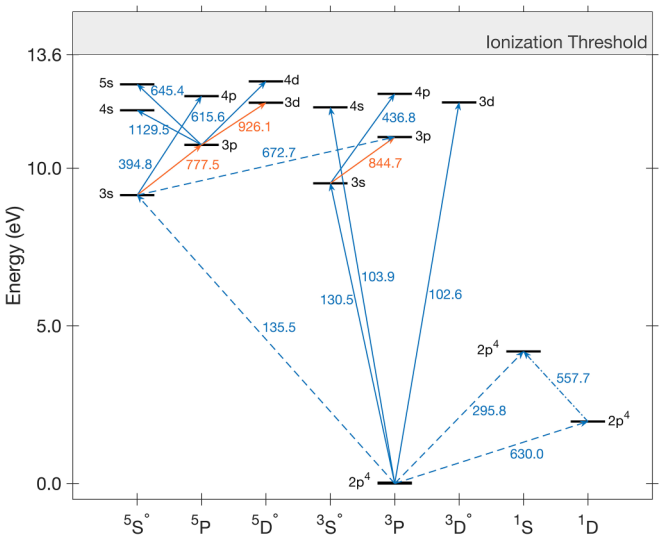

FIG. 1. Grotrian diagram of O I with absorption transitions leveraged for number density measurements marked with orange upward arrows. Wavelengths of the illustrated transitions are given in nm.

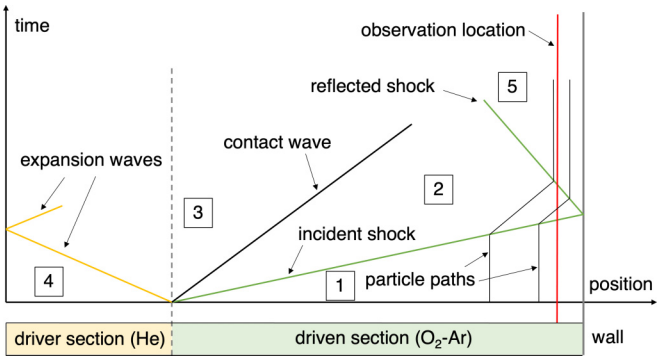

FIG. 2. Space-time diagram of the reflected shock experiments being analyzed. Regions are labeled using numbers, and dominant wave systems are labeled using colored lines.

els; however, these models lacked the necessary fidelity to fully describe the system behavior. In this paper, the experiments are studied using a detailed state-resolved, or collisional-radiative (CR), model that is developed following a comprehensive review of the rate parameters available to model each process. The developed model enables an in-depth study of the observed excitation dynamics, improving upon the current understanding of excited state oxygen kinetics and informing the interpretation of future excited state measurements.

The probed states are the fourth, fifth, and sixth excited levels of atomic oxygen, seen in Fig. 1 with orange arrows indicating the wavelength of laser radiation used to measure their populations. These states are radiatively and collisionally coupled to a large number of other electronic levels at both higher and lower energies. Because the states are close to the continuum, they are also strongly affected by ionization processes. Due to the large number of transitions involving the measured states, it is not intuitively obvious which ones are the most important to predictions of the measured states. To address this, a large-scale sensitivity analysis involving several hundred rate parameters is performed to isolate which processes most strongly influence the populations in the measured states.

The paper begins with a description of the shock tube flow modeling approach, followed by a thorough discussion of the developed collisional-radiative model. Next, the model is assessed and refined using measurements from shock tube experiments that probe the number densities of O_2, electrons, and three different atomic oxygen electronic states. The sensitivity analysis methodology and results are then presented and discussed, followed by a summary and conclusion.

II. GOVERNING EQUATIONS

All of the analyzed experiments are performed in pressure-driven shock tube facilities behind reflected shocks. A space-time diagram of the reflected shock wave system is shown in Fig. 2. Numbers are included to denote the various Regions that are separated by the waves emanating from the diaphragm rupture at the origin of the x-t diagram. One advantage of reflected shock experiments is that the stagnation of the test gas in Region 5 enables increased time resolution compared to incident shock experiments where the gas is typically advecting downstream at several kilometers per second. The experimental measurements of excited oxygen atoms, collectively referred to as O*, were performed in test gas mixtures of 99% argon and 1% O_2. Argon dilution allows for higher temperatures to be maintained throughout the test time without significant energy loss to dissociation or vibrational excitation.

The shock tube experiments are simulated via spatial integration of the one-dimensional steady Euler equations given in Eq. (1) in the reference frame of the reflected shock

$$\frac{d}{dx}\begin{bmatrix}\rho_p u\\ \rho u^2+P\\ \rho u(h+\frac{1}{2}u^2)\\ \rho u e_{\text{vib}}\\ \rho u e_{eex}\end{bmatrix}=\begin{bmatrix}m_p\omega_p\\ S_{m,dP}\\ -Q_{\text{rad}}+\rho S_{h,dP}\\ S_{\text{vib}}\\ S_{eex}\end{bmatrix}, \tag{1}$$

where x is the distance downstream of the shock, u is the flow velocity in the reflected shock reference frame, ρ_p is the density of pseudospecies p, m_p is the mass of a particle of pseudospecies p, P is the pressure, ρ is the total mass density, h is the specific enthalpy, e_{vib} is the specific vibrational energy, and e_{eex} is the specific electron-electronic energy. A pseudospecies is a general class of particles that evolves via its own continuity equation; pseudospecies in the current work encompass both species and individually resolved electronic states. The pseudospecies in the present model include the individual electronic states of O_2, O, Ar, and Ar^+, as well as the species O^+, O_2^+, and e^-. The specific electronic states being considered are specified in Sec. III A. The source terms are given on the right-hand side of Eq. (1) and include ω_p, the pseudospecies source term, Q_{rad}, the rate of radiative energy loss, $S_{m,dP}$ and $S_{h,dP}$, the momentum and energy source terms due to nonideal pressure rise, S_{vib}, the vibrational energy source term, and S_{eex}, the electron-electronic energy source term.

The vibrational energy, e_{vib}, is calculated using the Boltzmann fractions evaluated at T_{vib} for each vibrational state. Electron-electronic energy, e_{eex}, is the sum of the free electron energy given by $e_e = n_e k_B T_{eex}$ and the energy of the bound electronic states that are not explicitly tracked in the collisional-radiative model. For the present model, this includes the electronic states of O_2^+ and O^+, which are assumed to be Boltzmann populated at T_{eex}. The electronic energy, e_{ex}, which refers to the energy of the individually tracked electronic states, is directly calculated using the populations of each electronic state.

Endothermic processes in the gas behind a reflected shock can lead to significant deceleration of the reflected shock due to the density increases and cooling of the gas [12]. In the experiments analyzed in the present study, the test gas is 1% oxygen in argon. Dilution in argon is performed to minimize the test gas temperature and density changes caused by endothermic vibrational relaxation and dissociation of the O_2. Because the density change is negligible in the analyzed experiments, shock deceleration may be reasonably neglected and the initial condition of the test gas at the measurement location can be approximated using the reflected shock velocity that is calculated from the measured incident shock velocity and the no penetration boundary condition at the end wall.

A source term, $S_{m,dP}$, is introduced to the right-hand side of the momentum equation to ensure that pressure in Region 5 remains constant, a condition which is expected in the limit of weak Region 2 flow gradients [13] like those of the analyzed experiments. The momentum equation is reduced to $dP/dx = 0$ by setting the momentum source term to $S_{m,dP} = \rho u(du/dx)$ as derived by Baluckram *et al.* [14].

In real reflected shock experiments, the pressure often increases linearly throughout the test time. To incorporate a nonideal pressure rise in the momentum equation, a second term is added to the momentum source term that imposes the desired pressure behavior,

$$S_{m,dP} = \frac{d}{dx}(\rho u^2) + \frac{1}{u}\left(\frac{dP}{dt}\right)_{\text{meas.}}, \tag{2}$$

where the factor of $1/u$ accounts for the transformation of spatial to temporal coordinates $dx = udt$ and $(\frac{dP}{dt})_{\text{meas.}}$ is the measured nonideal pressure rise. Note that $S_{m,dP}$, as defined in Eq. (2), reduces the momentum conservation equation to $dP/dx = 1/u(dP/dt)_{\text{meas.}}$.

Due to the fast timescales of the experiment, pressure changes are modeled as isentropic compression as in [12,15]. Energy addition due to nonideal pressure rises is therefore given by $dh = \nu dP$, where $\nu = 1/\rho$ is the specific volume. The resulting energy source term due to nonideal pressure rise, $S_{h,dP}$, is

$$S_{h,dP} = \left(\frac{dP}{dt}\right)_{\text{meas.}}. \tag{3}$$

A. Energy mode coupling

Four pools of energy are considered in the present model: heavy particle translational-rotational, vibrational, electron-electronic, and the electronic energy of the individually resolved electronic states. The electronic energy is handled via a system of master equations and its treatment is described in Sec. III. Vibrational and electron-electronic energies are modeled using the mode approximation discussed in Sec. I and evolve through the solution of their own conservation equations that are detailed in this section.

TABLE I. Selected vibrational-translational relaxation time, τ_{vt}, expressions for O_2.

Collider	$P\tau_{vt,s}$ (atm-s)	Ref.
Ar	$4.7\times10^{-15}\exp\left(\frac{200}{T_{\text{tr}}^{1/3}}\right)\frac{T_{\text{tr}}^{5/6}}{1-\exp(-\frac{2240}{T_{\text{tr}}})}$	[15]
O_2	$8.4\times10^{-15}\exp\left(\frac{170}{T_{\text{tr}}^{1/3}}\right)\frac{T_{\text{tr}}^{5/6}}{1-\exp(-\frac{2240}{T_{\text{tr}}})}$	[15]
O	$1.85\times10^{-8}\exp(2.08\times10^{-5}T_{\text{tr}})$	[19][a]

[a]The Millikan and White correlation [20] is used for temperatures below 3000 K [21].

1. *Vibrational energy*

Vibrational energy evolves through relaxation with the heavy particle and free electron translational modes and through chemical reactions:

$$\rho u\frac{de_{\text{vib}}}{dx} = S_{\text{vib}} = -S_{ev} + S_{vt} + S_{vc}. \tag{4}$$

Electron-vibrational relaxation, S_{ev}, is modeled using the Bethe-Teller equation [16],

$$S_{ev} = \sum_{s\in\mathcal{M}} n_s \frac{\varepsilon_{vib,s} - \varepsilon^e_{vib,s}}{\tau_{ev,s}}, \tag{5}$$

where $\mathcal{M}$ is the set of molecular species and $\tau_{ev,s}$ is the electron-vibrational relaxation time modeled using the expression from Laporta *et al.* [17]. The average vibrational energy per particle of a species s is $\varepsilon_{vib,s}$, and $\varepsilon^e_{vib,s}$ is the average vibrational energy per particle of s evaluated at T_{eex}.

The source term for vibrational-translational relaxation, S_{vt}, is also calculated using the Bethe-Teller equation,

$$S_{vt} = \sum_{s\in\mathcal{M}} n_s \frac{\varepsilon^h_{vib,s} - \varepsilon_{vib,s}}{\tau_{vt}}, \tag{6}$$

with the mixture averaged vibrational relaxation time, τ_{vt}, calculated following Gnoffo *et al.* [18] with the collider-specific vibrational relaxation times given in Table I. There are several vibrational-translational relaxation times available for the interactions of the different species considered here [14]. Experimentally derived relaxation times are used for O_2-O_2 and O_2-Ar relaxation [15], while O_2-O relaxation is modeled using the relaxation time of Grover *et al.* [19].

Vibrational relaxation is strongly affected by the choice of vibration-dissociation coupling model for the dissociation of O_2. In several of the analyzed experiments, the vibrational temperature remains suppressed below T_{tr} for the entire test time. This vibrational nonequilibrium affects the rate of dissociation, which must be modeled accurately to enable meaningful comparisons with the excited state data. Based on recent experimental and computational studies of O_2 dissociation [12,15,22], the modified Marrone and Treanor (MMT)

TABLE II. Cross sections for electron-neutral collision cross section used in Eq. (9) and the temperatures over which they have been fit.

Species, s	$\sigma_{e,s}$ (10^{-20} m^2)	Temperature (K)	Ref.
Ar	$0.08156[\ln(T_{eex})]^3 - 1.166[\ln(T_{eex})]^2 + 3.678[\ln(T_{eex})] + 4.055$	300–40 000 K	Fit to [28]
O	$-0.01011[\ln(T_{eex})]^3 + 0.2431[\ln(T_{eex})]^2 - 1.260[\ln(T_{eex})] + 2.142$	300–50 000 K	Fit to [29]
O_2	$2 + (6\times10^{-4})T_{eex}$	5000–15 000 K	[18]

model with variable non-Boltzmann (VNB) correction is used to model the vibration-dissociation coupling in O_2-O_2, O_2-O, and O_2-Ar collisions using the rate coefficients and MMT model parameters from [6,15]. Extension of the MMT-VNB model for excited state dissociation is discussed in Sec. III B 3. For nondissociation reactions, molecular species are assumed to be created and destroyed at the average energy of that species [23]. This applies to associative ionization, charge exchange, and electronic excitation exchange reactions. The resulting expression for the vibrational energy change due to chemical reactions, S_{vc}, is

$$S_{vc} = \sum_{s\in\mathcal{M}} \sum_{i}^{n_{ex}} \sum_{r}^{n_r} \langle \varepsilon_{\text{vib}} \rangle_r \omega^r_{s(i)}, \tag{7}$$

where n_{ex} is the number of excited states of a molecular species s and n_r is the number of chemical reactions. The source term for a species s in electronic state i due to reaction r is $\omega^r_{s(i)}$. The average vibrational energy of the $s(i)$ molecules created or destroyed in a reaction r is $\langle \varepsilon_{\text{vib}} \rangle_r$.

2. Electron-electronic energy

The electron-electronic energy evolves through relaxation with the other energy modes, chemical reactions, and radiative emission. Unlike the vibrational mode, the electron-electronic energy mode is influenced by radiative processes, electronic excitation, and ionization. Exchanges between the electron-electronic energy mode and the energy of the individually resolved electronic states is mediated by electron impact excitation (S_{e-cie}) and ionization (S_{e-cii}) source terms, while radiative losses are captured in the free-bound (S_{fbr}) and free-free (S_{ffr}) radiative emission source terms. Changes to the electron-electronic energy during chemical reactions are accounted for in the S_{ec} source term:

$$\begin{aligned} \rho u \frac{de_{eex}}{dx} &= S_{eex} \\ &= S_{et} + S_{ev} + S_{e-cie} + S_{e-cii} - S_{fbr} - S_{ffr} + S_{ec}. \end{aligned} \tag{8}$$

The relaxation term between electron and translational-rotational energy, S_{et}, is given as

$$S_{et} = \frac{3}{2} k_B (T_{\text{tr}} - T_{eex}) \sqrt{\frac{8 k_B T_{eex}}{\pi m_e}} \sum_{s\in\mathcal{H}} \frac{2m_e}{m_s} n_e n_s \sigma_{e,s} (1 + g_{r,s}), \tag{9}$$

where $\sigma_{e,s}$ is the momentum-transfer cross section for electron-heavy particle collisions [24], and $g_{r,s}$ is the rotational loss factor used in [25]. The values of g_{r,O_2} and g_{r,O_2^+} are set to 10.0, a value first used in [26] for N_2 and later used for O_2 by [27] based on the similar rotational excitation cross sections of the two species. Rotational loss factors are zero for the atomic species. Momentum transfer cross sections for Ar and O collisions with electrons are taken from the B-Spline R-Matrix (BSRM) calculations presented in [28] and [29]. The momentum transfer cross sections that were calculated in both studies are in close agreement with previous experimental cross-sectional measurements. Equation (9) requires a cross section that is a function of temperature, not collision energy, so the energy-dependent cross sections are averaged over a Maxwellian electron energy distribution function at T_{eex} following [30] to arrive at the temperature-dependent expressions in Table II. For argon, the BSRM momentum transfer cross section is for the ground state, while for oxygen, the cross sections are reported for the ^3P, ^1D, and ^1S states. The state-specific oxygen cross sections are summed using the Boltzmann fraction in each state at T_{eex} to compute $\sigma_{e,O}$.

Electron-ion cross sections are treated using the Debye cutoff approximation, which leads to Eq. (10) from [31] with the factor of 4/3 implemented by [32]

$$\sigma_{e,s} = \frac{4}{3} \frac{4.39\times10^{-10}}{T_{eex}^2} \ln\left(\frac{1.24\times10^7 T_{eex}^{1.5}}{\sqrt{n_e}} \right) \quad [\text{m}^2]. \tag{10}$$

Relaxation between the free electrons and the individually resolved electronic states in Eq. (8) are mediated by $S_{e\text{-}cie}$ and $S_{e\text{-}cii}$, which represent the electron energy change due to collisionally induced electronic excitation and ionization by electron impact. The expressions for $S_{e\text{-}cie}$ and $S_{e\text{-}cii}$ have been reported by several authors including Jo *et al.* [1] and Aiken [33].

The electron translational energy decreases over time due to free-bound and free-free, or bremsstrahlung, emission. The gas is assumed to be optically thin to free-free emission, and emission due to radiative and dielectronic recombination to the ground state of argon is assumed to be completely self-absorbed due to the high concentration of ground-state argon atoms. Radiation from free-bound radiative transitions to excited state argon atoms is assumed to completely escape the gas based on the low concentration of excited argon atoms [24,34]. All free-bound emission involving recombination of an O^+ atom is also assumed to escape the gas completely [35]. Electron-electronic energy source terms due to free-bound source terms are elaborated in [33] and free-free radiative losses are modeled using the expressions from [9,24].

The final term in the electron translational energy equation is S_{ec}, the source term due to chemical reactions defined in Eq. (11),

$$\begin{aligned} S_{ec} = &\sum_{s\in\mathcal{H}_\mathcal{B}} \omega_s \varepsilon_{eex,s} + \omega_e^{\text{AI}} \varepsilon_{eex,e} \\ &+ \sum_{s\in\mathcal{M}} \sum_{i}^{n_{ex}} \omega^{\text{diss},e}_{s(i)} (D_{0,s(i)} - \varepsilon_{\text{rot},s(i)} - \varepsilon_{\text{vib},s(i)}), \end{aligned} \tag{11}$$

TABLE III. Species and excited states considered in the present model.

Species	Electronic states	Ref.
O_2	$X\,^3\Sigma_g^-$, $a\,^1\Delta_g$, $b\,^1\Sigma_g^+$, $c\,^1\Sigma_u^-$, $A'\,^3\Delta_u$, $A\,^3\Sigma_u^+$, $B\,^3\Sigma_u^-$	–
O	^3P_J, $^1D_2$, $^1S_0$, $^5S^\circ$, $^3S^\circ$,...(40 levels)	[35]
Ar	$^1S_0$, $^2[3/2]_2^\circ$, $^2[3/2]_1^\circ$, $^2[1/2]_0^\circ$, $^2[1/2]_0^\circ$,...(31 levels)	[24]
O^+	$^4S_{3/2}$, $^2D^\circ$, $^2P^\circ$, ^4P, ^2D	–
O_2^+	$X\,^2\Pi_g$, $a\,^4\Pi_u$, $A\,^2\Pi_u$, $b'^4\Pi_g$, $b\,^4\Sigma_g^-$	–
Ar^+	$^3P_{3/2}^\circ$, $^2P_{1/2}^\circ$	[24]
e^-	–	–

where $\mathcal{H}_B$ is the set of heavy species with electronic states that are assumed to follow a Boltzmann distribution at the electron-electronic temperature, ω_e^{AI} is the source term for electrons due to associative ionization and $\omega_{s(i)}^{\mathrm{diss},e}$ is the source term for $s(i)$ molecules due to electron impact dissociation. Species in $\mathcal{H}_B$ are assumed to be created or destroyed at the average electron-electronic energy of that species, $\varepsilon_{eex,s}$. For electron impact dissociation, molecules are assumed to be created or destroyed at the average rotational and vibrational energy. The average loss of electron translational energy during dissociation of a molecule $s(i)$ is thus the difference between the dissociation energy of the $s(i)$ molecule, $D_{0,s(i)}$, and the average rovibrational energy of an $s(i)$ molecule, $\varepsilon_{rot,s(i)} + \varepsilon_{vib,s(i)}$.

III. COLLISIONAL-RADIATIVE MODEL

A. Atomic and molecular model

The developed collisional-radiative model is designed for studying shock tube experiments in O_2-Ar mixtures from 5000 to 14 000 K and at pressures ranging from 0.15 to 1 atm. Dissociation and ionization are significant under these conditions, motivating consideration of the seven species listed in Table III.

The six electronic states of O_2 below the $O_2(X)$ dissociation limit are considered, along with the $O_2(B\,^3\Sigma_u^-)$ state that is involved in the Schumann-Runge system. The state grouping scheme for atomic oxygen was originally implemented by Bourdon *et al.* [35] and has also been used in [36,37]. The state grouping scheme enables accurate predictions of the net ionization and recombination rates, which require the resolution of electronic states close to the ionization limit. The excited states of the molecular and atomic oxygen ions listed in Table III are assumed to be Boltzmann populated at T_{eex}; i.e., $\mathcal{H}_B = \{O^+, O_2^+\}$.

The state model from Kapper and Cambier [24] is implemented for the electronic states of atomic argon and includes the first 31 states of Ar, ungrouped, and neglects all higher excited states. Excited states of the argon atom can have one of two core configuration quantum numbers, j_c, equal to either 3/2 or 1/2. It is assumed that the argon atom in a given electronic level is ionized to the Ar^+ excited state with the same j_c following [24,34]. Two excited states of Ar^+ must be considered to incorporate this effect.

Table III represents 83 pseudospecies conservation equations that are considered in the collisional-radiative model. The considered species and their excited states interact through a wide variety of collisional and radiative elementary processes that are described in Secs. III B and III C, respectively.

B. Collisional processes

Collisional processes can be mediated by a heavy particle or electron and include collision-induced excitation (CIE), collision-induced ionization (CII), and chemical reactions.

1. Electron-induced processes

Electrons dominate the excitation kinetics when their number density and average translational energy are sufficiently high, as is the case in many hypersonic flows at velocities exceeding those of Earth orbit. As a result, electron impact excitation and ionization (E-CIE and E-CII) have been studied extensively in previous works [35,38,39], and several complete data sets of electron impact cross sections exist for air species and argon [28,29,40–42]. Experimental cross-sectional measurements have been performed at a wide variety of collision energies for excitation and ionization involving select states of Ar and O; however, the measurement uncertainties are often large, complicating the validation of computational predictions [43].

In the present model, the cross sections calculated in [28] and [29] are integrated over a Maxwellian electron energy distribution, and the resulting rate coefficients are implemented. These data cover the electron impact excitation transitions involving the lowest 19 states of Ar and the lowest 11 states of O. Electron impact transition rates involving higher atomic levels are approximated using the fit to the Drawin [44] cross section presented in [37]. The E-CIE of O_2 is treated using the cross sections collected by Park [42], integrated over a Maxwellian electron energy distribution. Annaloro and Bultel's analytical rate expression is used for the remaining E-CIE transitions in O_2 [45]. The excitation rate coefficient between the two fine-structure levels of Ar^+ is calculated using the cross sections published by Kwon and Cho [46].

Electron impact ionization rate coefficients for the metastable states of atomic oxygen are calculated using the Arrhenius forms presented in [36], and the ionization rate coefficients for ground-state argon are calculated using the cross sections published by [28]. Ionization rate coefficients for the higher electronic states of O are approximated using the rate expression given in [25]. Electron impact ionization rate coefficients for the excited states of Ar are calculated using the cross-sectional formula and associated parameters from Deutsch *et al.* [47,48]. The rate coefficient expressions

TABLE IV. Selected rate coefficients for heavy particle impact excitation. The symbol M indicates the colliding heavy particle.

Species	i	j	M	Type	T (K) or ϵ (eV)	Ref.
O	1	2	O	$\sigma(\epsilon)$	2–10 eV	[49,50]
	1	2	Ar	k_Q	195–673 K	[51]
	1	2	O_2	k_Q	195–673 K	[51–53]
	1–2[a]	3	O	$k(T)$	–	[54,55]
	1–2	3	Ar	k_Q	298 K	[56]
	2[b]	3	O_2	k_Q	255–375 K	[52]
	4	5	Ar	$\sigma(\epsilon)$	0–8 eV	[57]
	6	7	Ar	k_Q	298 K	[58]
	6	7	O_2	k_Q	298 K	[59]
		Remaining		$k(T)$	–	[54]
Ar	1	$\{j \mid A_{1j} > 0\}$	All	$k(T)$	10 000–11 200 K	Present work
	2–4	3-5	All	$k(T)$	–	[24,34]
		$\{(i, j) \mid A_{ij} > 0\}$	All	$k(T)$	–	[60]
	10	11	Ar	k_Q	298 K	[61]
	7	8	Ar	k_Q	298 K	[61]
		Remaining		$k(T)$	–	[54]
O_2	1	2	O	k_Q	700–1700 K	[62]
	1	2	O_2	k_Q	100–450 K	[63]
	1	2	Ar	k_Q	298 K	[64]
	1	3	O_2	k_Q	300–800 K	[65]
	1	3	Ar	k_Q	$k_Q = k_{Q,O_2(a)+\mathrm{Ar}}$	[64,66]
	2[c]	3	O	k_Q	700–1700 K	[62]
	2	3	O_2	k_Q	650–1650 K	[67,68]
	2	3	O_2	k_Q	298 K[c]	[66]
	2	3	Ar	k_Q	298 K	[69,70]
	2, 3	4	Ar	k_Q	298 K	[66,71]
	3	4, 5, 6	O, O_2	k_Q	298 K	[66]
	3	5, 6	Ar	k_Q	$k_Q = k_{Q,O_2(c)+\mathrm{Ar}}$	[66,71]
		Remaining		$k(T)$	–	[54]

[a]Excitation of $O(^3P \rightarrow {}^1S)$ and $O(^1D \rightarrow {}^1S)$ by $O(^3P)$ are treated using Lemal's analytical formula instead of quenching rates because $O(^1S) + O(^3P)$ leads to $O(^1D) + O(^1D)$ [55].

[b]$1 \rightarrow 3$ is neglected since the product channel for $O(^1S) + O_2(X)$ leads to $O(^3P) + O_2(A,a,c)$ [52,72].

[c]Volynets *et al.* [62] did not report a definite product channel for the quenching of $O_2(b)$, but [70] found that most quenching partners de-excite $O_2(b)$ to form $O_2(a)$, and not $O_2(X)$.

[d]Park [66] assumes a constant value of $\sigma(\epsilon)$ for optically forbidden transitions when extrapolating room temperature quenching data.

published by Teulet *et al.* [41] are applied for the ionization of O_2 excited states by electron impact. The selected rate coefficients for dissociative recombination and dissociation by electron impact are discussed in Sec. III B 3.

2. *Heavy-particle-induced processes*

Heavy particle impact excitation (HP-CIE) and ionization (HP-CII) have received considerably less attention than the corresponding processes involving electrons, particularly at the high temperatures relevant to hypersonic flows. Table IV presents an overview of the HP-CIE rate constants and cross sections implemented into the model and the temperature or energy range over which they were measured, calculated, or inferred.

A small number of computational studies of HP-CIE or quenching have been performed for the species considered here, most of which are concerned with comparisons to experimental quenching rate coefficients at low temperature [73–75]. One exception is the excitation of $O(^3P \rightarrow {}^1D)$ via collisions with $O(^3P)$, studied in [49] and [50] using one-dimensional quantum scattering calculations for collision energies, ϵ, from threshold to 10 eV. Another exception is the cross-sectional calculation for $O(^3P) + O(^3P) \rightarrow O(^1D) + O(^1D)$ in [76].

Experimental cross sections of HP-CIE are also very scarce. To the authors' knowledge, the only published experimental cross sections for HP-CIE of atomic oxygen are given in [77] for excitation between the $^5S^\circ$ and $^3S^\circ$ states under impact by O_2, N_2, Ar, and Xe. The cross sections for excitation by collision with O_2 and Ar are integrated to obtain the rate constants that are implemented into the model. Rate constant expressions derived from the results of the aforementioned computational and experimental studies are given in Table V.

Many other relevant HP-CIE transitions have been studied in the vast literature devoted to determining rate coefficients for quenching, the reverse of HP-CIE; however, the rate constants are typically measured at room temperature. If a temperature dependence is determined, it is typically valid only below 1000 K [53]. Where available, quenching rates for O and O_2 are implemented into the present model. Table IV provides the temperature or range of temperatures at which

TABLE V. Arrhenius parameters for integrated theoretical and experimental cross sections [$k = AT^n \exp(-\theta/T)$].

Reaction	A (m^3/s)	n	θ (K)	Ref.
$O(^3P) + O(^3P) \rightarrow O(^3P) + O(^1D)$	1.37×10^{-19}	0.4546	21 506	[50]
$O(^3P) + O(^3P) \rightarrow O(^1D) + O(^1D)$	6.10×10^{-18}	0.0158	46 044	[76]
$O(^5S^\circ) + O_2(X) \rightarrow O(^3S^o) + O_2(a)$[a]	3.32×10^{-18}	0.0219	16 009	[77]
$O(^5S^\circ) + Ar \rightarrow O(^3S^o) + Ar$	3.12×10^{-19}	0.0448	9412	[77]

[a]Product assumed to be $O_2(a)$ based on the observed threshold energy.

each rate coefficient was determined. For the rate coefficients measured at 298 K that have no published temperature dependence, the rate coefficient is extrapolated by assuming that the cross section is constant with respect to collision energy. This results in quenching rate coefficients, k_Q, of the form $k_Q(T) = k_{Q,298K} \times \sqrt{\frac{T}{298K}}$; this extrapolation technique has also been applied in [66,78].

Most of the implemented rate coefficients for the HP-CIE of O_2 are taken from the review by Park [66], or from quenching rate coefficients collected by Capitelli *et al.* [52]. However, more recent data for the excitation of $O_2(X \rightarrow a)$ and $O_2(a \rightarrow b)$ in collisions with $O(^3P)$ are taken from the recent quenching experiments in [62] that probed temperatures up to 1700 K. Excitation occurs more rapidly using the newly determined rate coefficients, in comparison to the rate coefficients extrapolated from room temperature that are reported by Park.

Rate coefficients have been published only for electronic transitions in heavy particle collisions for the ground and metastable electronic states of O_2 and O. Calculating the excitation or quenching rate coefficients of higher-lying electronic states is often intractable due to the rapid increase of state density with energy. Experimentally, it is difficult to produce stable and long-lived populations of high-lying electronic states, many of which have very short radiative lifetimes. In the cases where removal rates have been measured, isolating product channels proves challenging due to the large number of energetically accessible removal pathways. For this reason, the majority of published removal rates for metastable argon are not implemented, with the exception of several from Sadeghi *et al.* [61] where the products are specified.

For the transitions where rate coefficient data are unavailable, several theoretical expressions are available to approximate the necessary HP-CIE rate constants [32,36,45,60]. These models offer convenient closed-form expressions for excitation rate constants between any two states; however, the rate coefficients predicted by the various models are spread across four orders of magnitude [1,54]. For the transitions of O_2 and O where no data are available, the cross-sectional expression from Park [32], given in Eq. (12), is adopted with the value of $\sigma_0 = 1.21\times10^{-24}$ m^2 based on findings from Lemal *et al.* [54]:

$$\sigma^{hp-cie}_{s(i,j)+M}(\epsilon) = \sigma_0 \left(\frac{\ln(\epsilon/\varepsilon_{ij})}{\epsilon/\varepsilon_{ij}} \right). \tag{12}$$

Several research groups studying argon ionization behind strong shock waves have inferred rate coefficients for excitation from $Ar(^1S)$ to the higher radiatively coupled levels. The cross-sectional scale factors inferred over the years have been tabulated in [24] and are scattered across nearly two orders of magnitude. In the present work, the rate coefficients for these transitions are determined by scaling the rate coefficients used by Kapper and Cambier [24] to match measurements of electron number density in 1% mixtures of O_2 dilute in argon. Excitation rates involving the 4*s* states of argon are modeled using the rate coefficients from Kapper and Cambier, and Drawin's formula is used for HP-CIE between pairs of radiatively coupled excited states of argon [24,34]. For the HP-CIE between excited states of argon that are not radiatively coupled, the logarithmic cross section suggested by [54] is implemented.

Experimentally measured cross sections for ionization in the impact of two ground-state argon atoms are implemented from [79]. Heavy particle impact ionization of the excited levels of argon is modeled using the expression from Drawin and Emard [60]. Heavy particle impact ionization of O and O_2 is modeled using the rate coefficient expression from Annaloro and Bultel [45],

$$k^{hp-cii}_{s(i,j)+M} = \sqrt{\frac{8k_bT_{tr}}{\pi\mu}}\sigma_0 a_1 \left(\frac{-\varepsilon_{ij}}{k_BT_{tr}}\right)^{a_2} \exp\left(\frac{-\varepsilon_{ij}}{k_BT_{tr}}\right), \tag{13}$$

where $a_1 = 0.39534$, $a_2 = 0.3546$, and μ is the reduced mass of the colliding particles. The scale factor, σ_0, is set to 1.21×10^{-24} m^2 instead of Annaloro and Bultel's suggested 10^{-20} m^2 based on the findings by Lemal *et al.* [54] for the appropriate magnitude of HP-CIE reactions in postshock flows.

3. Chemical reactions

Chemical processes included in the model are molecular dissociation, electronic excitation exchange and energy pooling, associative ionization, and charge exchange. The rate coefficients published by Chaudhry *et al.* [80] are used for the dissociation of $O_2(X)$ in collisions with O_2 and O, and those from Kim and Boyd [81] are used for the dissociation of the ground and first two excited states of O_2 in collisions with argon.

The rate coefficients from Kim and Boyd are for dissociation during the quasi-steady-state (QSS) period, a temporarily stable nonequilibrium state where dissociation and vibrational relaxation are balanced. Much of the dissociation behind strong shock waves occurs during the QSS phase [6], so the application of QSS rate constants in the present analyses is well justified. During QSS, the vibrational states closest to the dissociation limit are underpopulated with respect to a Boltzmann distribution at T_{vib} because the dissociation of these high-energy states occurs faster than vibrational excitation can repopulate them. As a result, the QSS dissociation

TABLE VI. O_2-Ar dissociation rate coefficient parameters [$k_d = AT^n \exp(-T_d/T)$].

Electronic state	A (m^3/s)	n	T_d (K)
$X\,^3\Sigma_g^-$	4.43×10^{-14}	−0.344	60 850
$a\,^1\Delta_g$	2.50×10^{-14}	−0.314	49 515
$b\,^1\Sigma_g^+$	2.99×10^{-14}	−0.333	41 892
$c\,^1\Sigma_g^-$	3.21×10^{-14}	−0.330	11 884
$A'\,^3\Delta_u$	3.21×10^{-14}	−0.330	10 014
$A\,^3\Sigma_u^+$	3.21×10^{-14}	−0.330	9021
$B\,^3\Sigma_u^-$	3.21×10^{-14}	−0.330	11 208[a]

[a]Dissociates to $O(^3P) + O(^1D)$.

rate coefficient is lower than that for Boltzmann-populated vibrational states at T_{vib}.

In the modified Marrone and Treanor model, the reduction of the dissociation rate at QSS is approximated by scaling the equilibrium dissociation rate constant by 0.5 [80]. Because the MMT model assumes that the inputted dissociation rate constant expressions are those valid for a Boltzmann vibrational-state distribution, the Kim and Boyd [81] rate constants for O_2+Ar dissociation are scaled by 2 to ensure that the desired rate constants are recovered at QSS. The MMT model constants U^* and a_U are set to 1/3 of T_d and zero, respectively, for O_2 dissociation with argon.

The rate coefficients for the dissociation of the Herzberg O_2 electronic states with argon are approximated by taking the geometric mean of the preexponential factors and the arithmetic mean of the temperature exponents for the $O_2(i$=X, a, b)+Ar dissociation rate constants. The electronic state-specific dissociation rate coefficients for O_2-Ar are given in Table VI.

A common approximation of excited state dissociation rate constants is to take the Arrhenius expression for the ground-state dissociation rate and change only the threshold to match the dissociation energy of the excited state while keeping the pre-exponential factor and temperature exponent unchanged. Using the O_2-Ar dissociation rate constants with O_2(X), O_2(a), and O_2(b), that approximation can be assessed. It is found that, over the range of 5000 K to 15 000 K, the dissociation rate constant for O_2(a) and O_2(b) with Ar is 73%–75% of what is predicted by merely changing T_d from the O_2(X) rate expression. As a result, the pre-exponential factors, A, on the O_2(X)+O and O_2(X)+O_2 dissociation rate constant expressions are scaled by 0.75 to approximate the excited state dissociation rate constants in Table VII.

Electron impact dissociation rate coefficients for O_2 are implemented from Park [42] and Teulet *et al.* [41]. The associative ionization to form O_2^+ is modeled using the cross-sectional expressions in [82]. Rate coefficient parameters for the three associative ionization channels are given in Table VIII.

TABLE VIII. Arrhenius rate parameters for the AI to form $O_2^+(X\,^2\Sigma_g^+)$ [$k = AT^n \exp(-\theta/T)$].

Reactant channel	A (m^3/s)	n	θ (K)
$O(^3P) + O(^3P)$	8.529×10^{-23}	1.00	77 170
$O(^3P) + O(^1D)$	1.621×10^{-21}	1.00	57 907
$O(^1D) + O(^1D)$	9.472×10^{-22}	1.00	35 045

Charge exchange rate coefficients are taken from [5] for O_2^+ + O and [83] for charge exchanges from Ar^+ to O and O_2. Excitation exchange and energy pooling reaction rates from Starik *et al.* [83] and Kossyi *et al.* [72] are implemented as well. Electronic excitation and energy pooling reaction cross sections are assumed to be constant when no temperature dependence for the rate coefficient is given, resulting in the same $\sqrt{T}$ scaling used to extrapolate quenching rates to the temperature range of interest. All equilibrium constants are determined using detailed balance [84,85].

C. Radiative processes

Molecular radiation from the Schumann-Runge band is included using the vibrational state-specific Einstein coefficients from [86]. For atomic oxygen and argon, all lines from the NIST database that involve the modeled states are included [87]. When the upper state for a given line is within a grouped state, the Einstein A coefficient is scaled by the ratio of the upper state electronic degeneracy to the total electronic degeneracy of its grouped state. This procedure is appropriate for the present model since all states in a given group are close in energy to one another. A total of 119 lines for O and 102 for Ar are considered.

Free-bound transition rates are implemented for atomic oxygen following Bourdon *et al.* [35], while the rates for argon are taken from Kapper and Cambier [24]. The medium is assumed to be optically thin to emission from radiative and dielectronic recombination to atomic oxygen and to excited state argon. Escape factors are calculated using Holstein's formula for an infinite slab [88,89], where the length scale is taken to be either 1.0 cm, the approximate length scale of flow gradients in the shock tube [90,91], or 15.24 cm, the diameter of the shock tube [8]. As a default, the self-absorption length scale, L_{rad}, is set to 1.0 cm. The effects of this choice on

TABLE VII. O_2-O_2 and O_2-O dissociation rate coefficient parameters [$k_d = AT^n \exp(-T_d/T)$]. The dissociation temperature of each state, $T_{d,i}$, is given in Table VI.

Interacting particles	A (m^3/s)	n	T_d (K)	a_U	U^* (K)
$O_2(X\,^3\Sigma_g^-) + O_2$	6.1327×10^{-12}	−0.7695	60 540	0.3965	57 343
$O_2(i > 1) + O_2$	4.5995×10^{-12}	−0.7695	$T_{d,i}$	0	$T_{d,i}/3$
$O_2(X\,^3\Sigma_g^-) + O$	1.5295×10^{-12}	−0.6541	60 552	0.3537	237 290
$O_2(i > 1) + O$	1.1471×10^{-12}	−0.6541	$T_{d,i}$	0	$T_{d,i}/3$

TABLE IX. Reflected shock experiments analyzed in the present study.

Name	$T_{5,0}$ (K)	$P_{5,0}$ (atm)	X_{O_2} (%)	ΔP_5 (%)	Time res. (μs)	Measured time histories	Ref.
Streicher-20-L	5280	0.45	2	2.2	1	T_{vib}, n_{O_2}	[22]
Streicher-20-M	8120	0.11	2	11.8	1	T_{vib}, n_{O_2}	
Streicher-20-H	10 710	0.04	5	11.1	1	T_{vib}, n_{O_2}	
Nations-16	7250	0.61	1	$\lesssim$1	10	$n_{O(^3S^\circ)}$, $n_{O(^5S^\circ)}$	[8]
Li-20-L1	8124	0.35	1	<12	20	$n_{O(^5S^\circ)}$	[9]
Li-20-L4	10 296	0.15	1	<12	20	$n_{O(^5S^\circ)}$	
Li-20-H2	9161	0.95	1	<12	20	$n_{O(^5S^\circ)}$	
Li-21-1	10 153	0.49	1	$\lesssim$ 6	20	n_e, $n_{O(^5P_3)}$, T_{tr}, $n_{O(^5S^\circ)}$	[10]
Li-21-2	10 623	0.44	1	$\lesssim$6	20	n_e, $n_{O(^5P_3)}$, T_{tr}, $n_{O(^5S^\circ)}$	
Li-21-3	10 923	0.33	1	$\lesssim$6	20	n_e, $n_{O(^5P_3)}$, T_{tr}, $n_{O(^5S^\circ)}$	
Li-21-4	11 209	0.37	1	$\lesssim$6	20	n_e, $n_{O(^5P_3)}$, T_{tr}, $n_{O(^5S^\circ)}$	
Minesi-1920	9525	0.32	1	19.3	0.2	T_{tr}, $n_{O(^5S^\circ)}$	[11]
Minesi-2037	12 199	0.23	1	26.1	0.2	T_{tr}, $n_{O(^5S^\circ)}$	

model comparisons with experimental data are discussed in Sec. IV D.

IV. COMPARISON WITH EXPERIMENT

A. Description of experiments

The present collisional-radiative model is assessed using a selection of the shock tube experiments presented in [8–11,22]. The conditions of the analyzed experiments are listed in Table IX. The Streicher, Nations, and Li experiments were all performed in the same shock tube with an inner diameter of 15.24 cm, while the Minesi data were measured in a separate shock tube with a 10.32 cm inner diameter. Data from the Nations-16 experiment were measured using cavity-enhanced absorption spectroscopy (CEAS), while the Streicher-20, Li-20, Li-21, and Minesi experiments used single-pass laser absorption spectroscopy (LAS). In all experiments, the measured absorbances were used to infer quantum state-specific number density time histories. In addition, T_{tr} is inferred from the Doppler broadening of the 777 nm line in the experiments from [10,11], and the Stark shift of the 926 nm line is used to infer electron number density in [10]. Stark broadening of the 777 nm line may also be used to infer n_e; however, uncertainty in the Stark coefficient means that n_e inferences from that line are highly uncertain [11,92].

The experiments in Table IX are a subset of the published experiments in which excited atomic oxygen number densities have been measured. Figure 3 illustrates the distribution of experimental conditions within temperature and pressure space, with the experiments selected for in-depth analysis marked in red. The three experiments from [22], which are used to validate the predictions of O_2 dissociation within the model, are shown in Fig. 3 as well.

The excited state measurements span a wide temperature range from 7000 to 12 000 K at pressures from 0.15 to 0.96 atm. The selected experiments for in-depth analysis are chosen based on their location in temperature-pressure space, the type(s) of measured time histories, and the time resolution of the measurement. This last consideration, the time resolution, is a major distinguishing feature of the data published by Minesi *et al.* [11], in addition to the higher temperatures probed.

Values for the nonideal pressure rise are not reported in [8–10]; those authors report low total pressure increases ranging from 1% [8] to 6% [9,10], accomplished through the use of a driver insert. In contrast, nonideal pressure rises are reported in the Minesi *et al.* experiments and range from 0.24 to 0.40 torr/μs, corresponding to total pressure rises of 19% to 31%.

B. O_2 number density

The dissociation of O_2 is an important process that significantly influences the predicted atomic oxygen excited state time histories. In several experiments, the dissociation of O_2 is nearly complete before the first laser scan is complete; however, in many cases, the excited state measurements are taken while O_2 dissociation is still ongoing. Measurements by

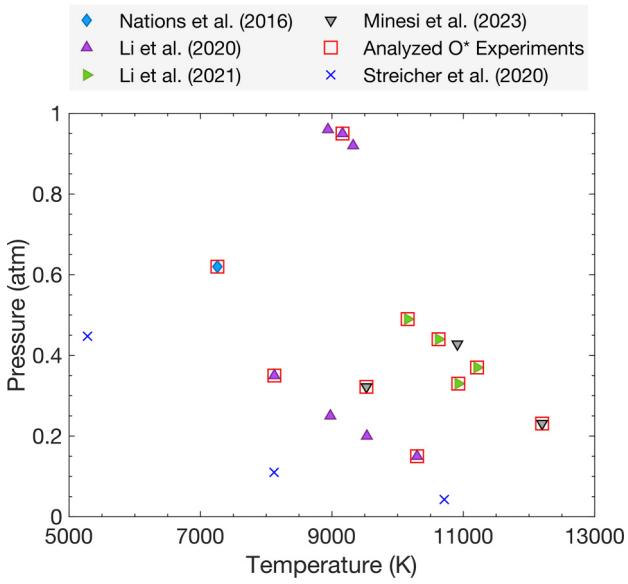

FIG. 3. Available and selected experimental conditions for measurements of excited atomic oxygen and ground-state molecular oxygen.

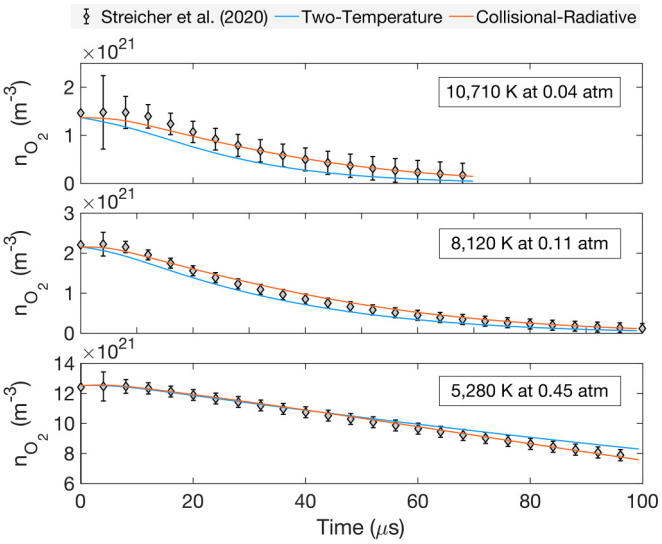

FIG. 4. O_2 number density predictions using the present collisional-radiative model alongside predictions from a two-temperature model using parameters from [22].

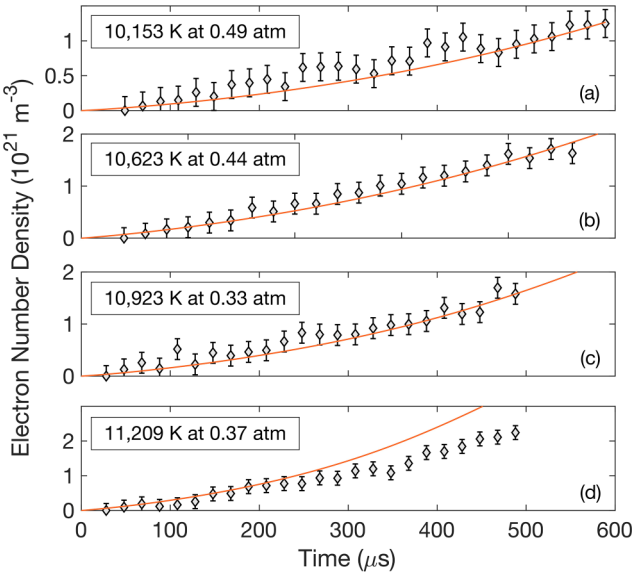

FIG. 5. Electron number density predictions by the collisional radiative model using the inferred rate constant expressions for $\mathrm{Ar}(1) + \mathrm{Ar} \leftrightharpoons \mathrm{Ar}(i) + \mathrm{Ar}$.

Streicher *et al.* [15,22] of the number density and vibrational temperature of $O_2(X)$ during vibrational relaxation and dissociation in mixtures of 2% to 5% O_2 in argon enable validation of the adopted O_2 dissociation model.

Predictions of O_2 dissociation by the collisional-radiative model are shown in Fig. 4. Two-temperature model predictions are also shown as a reference, calculated using the dissociation rates and relaxation times from [22]. The collisional-radiative model achieves excellent agreement with the measured O_2 number density time histories across the 5200–10 700 K range of temperatures. Results in Fig. 4 indicate that O_2 dissociation is effectively modeled in the adopted collisional-radiative model.

C. Electron number density

The net ionization rate is a primary determinant of the overall system behavior. The HP-CIE reaction $\mathrm{Ar}(1) + \mathrm{Ar} \leftrightharpoons \mathrm{Ar}(i) + \mathrm{Ar}$, where i is a level with strong radiative coupling to Ar(1), is the critical process influencing the electron number density across all analyzed experiments. The importance of these transitions to net ionization in shock-heated argon was discussed extensively by Kapper and Cambier [24]. To further assess whether the HP-CIE of Ar is the primary driver of electron formation, the observed threshold energy of ionization is deduced by linearly fitting the rise of n_e that is measured in the four Li-21 experiments. Linear regression of the fitted dn_e/dt values from each experiment yields a threshold of 12.6 eV with a standard error of 1.6 eV and an adjusted R^2 of 0.95. The fitted slope supports argon excitation, with a threshold of 11.55 eV, as the primary rate-limiting mechanism for ionization. This is consistent with the well-established observation that ionization in shock-heated argon is controlled by an 11.5 eV threshold, consistent with the electronic excitation of argon, rather than the 15.7 eV threshold for direct ionization from the ground state [93–96].

The accurate prediction of electron number density is a necessary prerequisite for making meaningful comparisons with the atomic excited state data analyzed in Sec. IV D. Given the importance of argon electronic excitation to the formation of electrons in the analyzed experiments, a straightforward improvement of the model may thus be realized by inferring a scale factor for the rate coefficients of $\mathrm{Ar}(1 \rightarrow i)$ heavy particle impact excitation using the electron number density measurements in the Li-21 experiments. A single scale factor of 55 is found to satisfactorily reproduce the measured electron number density in three of the four experiments, with the Li-21-4 experiment requiring a scale factor of 33. As a result, the excitation rate constants for the HP-CIE of $\mathrm{Ar}(1 \rightarrow i)$ are increased by a factor of 55, producing the model predictions shown in Fig. 5. Arrhenius expressions for the fitted $\mathrm{Ar}(1 \rightarrow i)$ excitation rate constants are provided in Table X.

In Fig. 6 the inferred rate constant for excitation of $\mathrm{Ar}(1 \rightarrow 5)$ is plotted against several rate constants from the literature. The inferred argon HP-CIE rate constant is faster

TABLE X. Excitation rate coefficient parameters for $\mathrm{Ar}(1) + \mathrm{Ar} \rightarrow \mathrm{Ar}(i) + \mathrm{Ar}$ inferred using the measured n_e data from [10]. The rate coefficients are scaled up by a factor of 55 from those reported in [24].

i	A (m^3/s)	n	θ (K)
3	1.8359×10^{-21}	0.7639	134 170
5	6.9124×10^{-21}	0.7606	136 540
17	2.5366×10^{-23}	0.7314	160 240
23	8.5725×10^{-22}	0.7286	162 870
25	2.3876×10^{-21}	0.7278	163 600
30	4.5150×10^{-22}	0.7267	164 790
31	1.9837×10^{-21}	0.7260	165 360

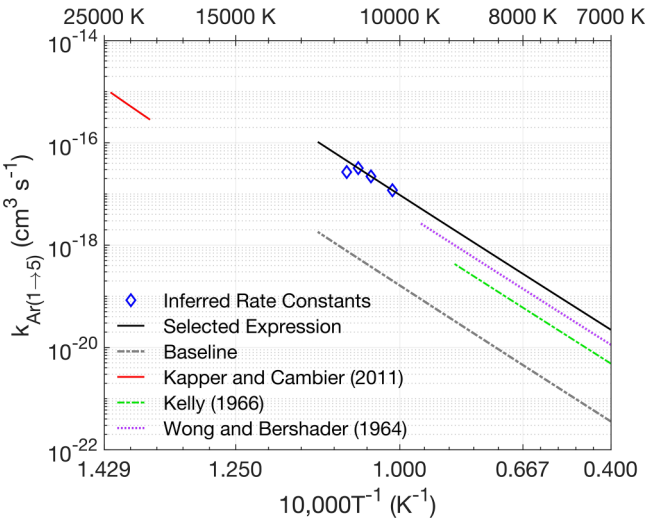

FIG. 6. Comparison of rate constants available for the electronic excitation of Ar(1 → 5) in Ar + Ar collisions.

than the baseline rate constant, which was fitted to experimental data at temperatures above 20 000 K by Kapper and Cambier [24]. The baseline rate coefficient from [24] is the lowest available rate constant from the literature, and several other authors have inferred rate constants that range from 2.5 to 28 times larger than Kapper and Cambier's inferred value. Harwell and Jahn [93] arrived at a rate constant that is 71 times larger than the baseline rate constant but subsequently revised their value down by a factor of ten, citing "equipment modifications" [96]. Thus, the largest published rate constant is that of Wong and Bershader [95], which is 28 times larger than the baseline value taken from Kapper and Cambier and 50% smaller than the rate expression adopted in the present model.

Several effects may explain the increased rate of ionization observed in the Li-21 experiments. For one, all of the literature rate constants presented in Fig. 6 were measured in experiments involving pure argon, while the Li-21 experiments contained 1% O_2. Notably, however, interferograms obtained by Glass and Liu [97] for argon test gasses with an O_2 impurity of 0.46% did not reveal a notable reduction of the ionization length compared to the pure argon experiments, indicating that the addition of O_2 does not appreciably impact the net ionization rate of the argon bath gas. In contrast, impurities containing hydrogen are known to strongly impact the ionization rate in pure argon experiments; Harwell and Jahn report that impurity levels of 1 part per million are sufficient to influence the measured ionization rate in their pure Ar experiments [93]. One part per million is an upper limit on the expected water vapor impurity in the shock tube where Li *et al.* performed their experiments [98], so it is unlikely that hydrogen impurities fully explain the observed rate; however, other impurities such as metallic or carbonaceous species may also be present.

Gas compression induced by nonideal pressure rises behind the reflected shock may also increase the ionization rate of the system. In their analysis of ionization rates behind incident shocks in argon, McLaren and Hobson [99] state that the inclusion of boundary layer growth and test gas compression via Mirels theory [100] has the effect of reducing the inferred argon excitation rates from Kelly [94] and Morgan and Morrison [96] by roughly a factor of three. When a dP/dt corresponding to the maximum 6% total pressure rise reported by Li *et al.* is implemented, the inferred Ar(1) + Ar → Ar(i) + Ar excitation rate is decreased by 30%. None of the aforementioned effects appear to be sufficient for explaining the discrepancy from previously inferred rate constants. The observed rate constant is likely influenced by a combination of these factors; thus, the adopted rate expression for the HP-CIE of Ar(1 → i) should be understood as an "effective" rate expression that subsumes the effects of argon electronic excitation, impurity ionization, and Region 5 gas compression. Further measurements of electron number density across wider ranges of temperature and pressure would help identify the key mechanisms explaining the enhanced ionization observed in the measurements by Li *et al.* [10] and further assess the validity of the adopted scale factor for the HP-CIE of Ar(1 → i).

While the inferred scale factor for Ar(1 → i) electronic excitation is a component of the model that ensures that predictions of electron number density are consistent with the available experimental data, it is not recommended for general adoption. The primary interest of the present study is to assess the modeling of the electronic excitation kinetics of atomic oxygen, which can only be effectively studied if the predicted levels of argon bath gas ionization are consistent with the available data. By adopting an "effective" rate coefficient for the HP-CIE of Ar(1), the other processes in the kinetic model can be effectively studied because ionization levels are known to be consistent with the available measurements.

D. Atomic oxygen electronic excitation

When analyzing the measured data for atomic oxygen excited states, rate constant inferences become considerably more complicated. The best information on individual rate constants may be derived not from measurements of individual electronic states but from the observed relationship between multiple simultaneously measured electronic states. Two experimental data sets provide simultaneous measurements of two electronic states: the Nations-16 and Li-21 experiments. The kinetics of the Nations-16 experiment are simpler than those of the Li-21 experiments because the former was performed at a low temperature where electron-driven processes are not significant contributors to the excited state dynamics.

One key parameter that may be derived using the measured populations of two excited states is the excitation temperature, $T_{ex,s(i,j)}$, defined by the ratio of populations in levels i and j of a species s where $j > i$. The excitation temperature is calculated via Eq. (14). The degeneracies, g, of the $^5S^\circ$ and $^3S^\circ$ states are 5 and 3, respectively. When using the measured O($^5P_3$) data from Li-21, the degeneracy is set to 7 since only the $J = 3$ state is measured. Otherwise, the total ^5P degeneracy is 15:

$$T_{ex,s(i,j)} = \left[\frac{k_B}{\varepsilon_{ij}} \ln\left(\frac{n_i/g_i}{n_j/g_j}\right)\right]^{-1}. \tag{14}$$

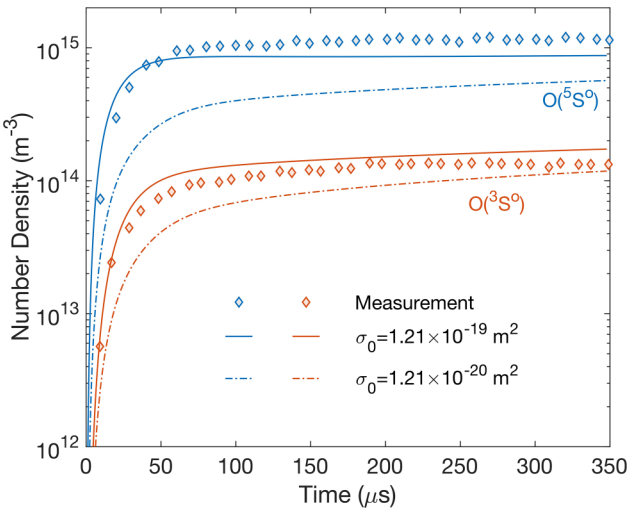

FIG. 7. Model predictions compared with experimental data from Nations-16 using two values of the cross-sectional scale factor σ_0 for the HP-CIE reaction $O(^3P) + Ar \rightarrow O(^5S^\circ) + Ar$.

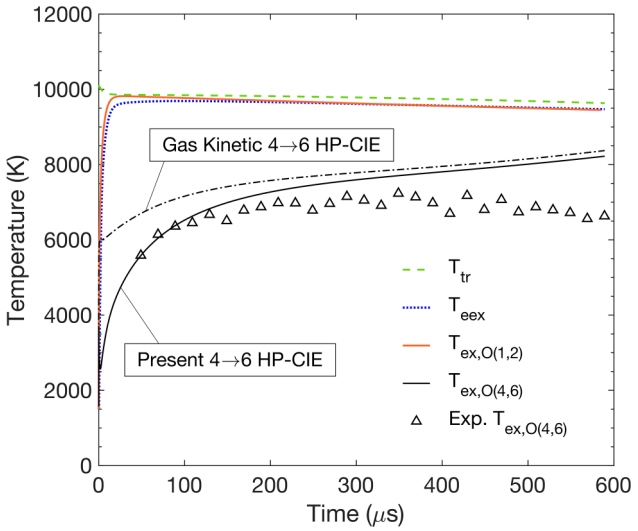

FIG. 8. Temperature predictions for the Li-21-1 experiment, including the electronic temperature for the fourth and sixth excited states of O as calculated from the measured data and the model predictions.

The Nations-16 experiment is the only one in which the $^3S^\circ$ state of oxygen is measured. Within the adopted model, the populations of the $^5S^\circ$ and $^3S^\circ$ states are controlled by a balance between collisional excitation and radiative transitions. For the $^5S^\circ$ state, the principal radiative transitions are with the sixth excited $3p$ ^5P state, while the principal transitions of the $^3S^\circ$ state involve the seventh excited $3p$ ^3P and ground $2p^4$ ^3P electronic levels. These interactions induce a coupling of the excitation temperatures $T_{ex,O(4,5)}$ and $T_{ex,O(6,7)}$, the former of which is measured in the Nations-16 experiment.

Energy-dependent cross sections for the excitation of $O(^5S^\circ)$ to $O(^3S^\circ)$ in collisions with argon have been measured by Kiefl and Fricke [57] from threshold to 8 eV. Dagdigian *et al.* and Piper have also measured the quenching rate of $O(3p\ ^3P \rightarrow 3p\ ^5P)$ in collisions with O_2 and argon, respectively, at room temperature [58,59]. The collisional couplings between the $^5S^\circ$ and $^3S^\circ$ states and between the $3p$ ^3P and $3p$ ^5P states are weak when these rate coefficients are adopted. Weak collisional coupling between the quintet and triplet states is consistent with the experimentally observed suppression of the excitation temperature $T_{ex,O(4,5)}$ throughout the test time. The value of $T_{ex,O(4,5)}$ stays between 2000 and 2700 K throughout the entire test time, much lower than the equilibrium temperature of 7039 K, indicating that the collisional excitation of $O(^3S^\circ)$ and $O(3p\ ^3P)$ is weak compared to the radiative de-excitation of these states to form to ground-state $O(2p^4\ ^3P)$.

Predictions of the collisional-radiative model are compared with the Nations-16 experimental data in Fig. 7. A major success of the present model is its accuracy in capturing the depressed $O(^3S^\circ)$ population relative to the measured $O(^5S^\circ)$ population. Model predictions are improved significantly by scaling up the rate coefficient for the HP-CIE reaction $O(^3P) + Ar \rightarrow O(^5S^\circ) + Ar$ by a factor of ten from the baseline value adopted from Lemal *et al.* [54]. Based on these results, the HP-CIE rate scaling for the $O(1 \rightarrow 4)$ rate constant is adopted throughout the remainder of the present work.

Experimental measurements in the Li-21 data set provide information on the coupling between the fourth and sixth excited states of O. In the original analysis of these data, the excitation temperature was found to quickly equilibrate with the translational temperature, indicating that the $^5S^\circ$ and ^5P levels are strongly coupled via heavy particle collisions. In the present work, reprocessing of the experimental data yields different results for $T_{ex,O(4,6)}$, and the original author has confirmed that an erroneous value was used for the $O(^5P)$ electronic degeneracy in their initial analysis [101].

The measured and predicted values of $T_{ex,O(4,6)}$ for the Li-21-1 experiment are shown in Fig. 8 alongside the electron and heavy particle translational temperatures. Results obtained using two rate constants for the heavy particle impact excitation reaction $O(^5S^\circ) + Ar \rightarrow O(^5P) + Ar$ are shown in the figure. The baseline rate, based on the recommended cross section of Lemal *et al.* [54], yields early-time predictions of $T_{ex,O(4,6)}$ that are consistent with the measured data. In contrast, when the $O(4 \rightarrow 6)$ excitation cross section is set to the hard-sphere cross section of the oxygen atom—assuming that every collision of $O(^5S^\circ)$ with Ar results in an excitation to $O(^3P)$; i.e. the gas kinetic limit—the excitation temperature of $O(4 \rightarrow 6)$ is much higher than the experimental data suggest. The rate constant inferred by Li *et al.* [10] for the HP-CIE excitation of $O(4 \rightarrow 6)$ is within a factor of 2 of the gas kinetic limit, while the rate constant used in the present model is four orders of magnitude smaller.

In the present model, the free electron temperature relaxes to the translational temperature much faster than the model adopted by Li *et al.* [10] predicts. The fast relaxation is caused by rapid energy transfer between the heavy particle and electron translational modes that is mediated by $O(^1D)$, a state that is not included in the model of Li *et al.* First, $O(^1D)$ is formed in O + O and O + Ar collisions, quickly bringing the ^1D state to equilibrium with the heavy particle translational temperature, illustrated using the $T_{ex,O(1,2)}$ line

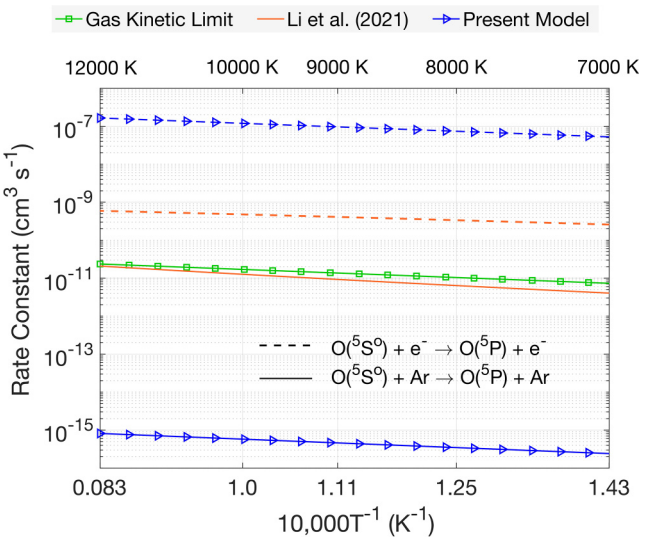

FIG. 9. Rate constants for the excitation of O(4 → 6) in collisions with argon and electrons. The E-CIE rate constant from Li *et al.* [10] is the baseline rate constant in that study. The HP-CIE rate from Li *et al.* is the optimized rate constant obtained by multiplying their baseline value by 6,200.

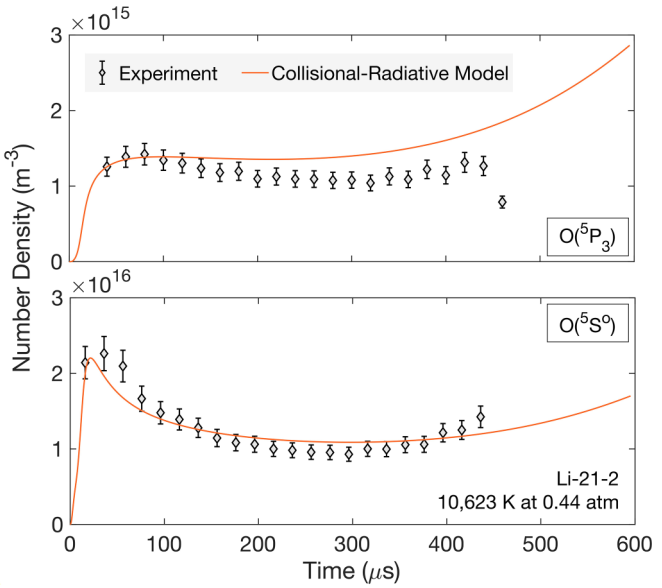

FIG. 10. Comparison of collisional-radiative model predictions with measured data from the Li-21-2 experiment. Agreement with the experimental data is representative of other experiments in the Li-21 data set.

in Fig. 8. The large population of O(^{1}D) then serves as an energy reservoir from which the electrons gain translational energy via superelastic scattering in the de-excitation reaction O(^{1}D) + e$^-$ → O(^{3}P) + e$^-$. For this reason, the free electron translational temperature, T_{eex}, follows closely behind $T_{ex,O(1,2)}$ and quickly rises to a quasi-steady state value that is approximately 400 K below $T_{\rm tr}$.

Rapid relaxation of the free electron temperature is a major change to the overall system kinetics that arises from including the metastable states of oxygen and the best available rate constants for the heavy-particle impact excitation of those states. It is recommended that the metastable atomic electronic states be included in future interpretations of measured data for high-lying atomic electronic states in shock tube experiments.

By including the kinetics of the O(^{1}D) state, the present analysis arrives at a much slower rate coefficient for the HP-CIE of ^{5}S$^\circ$ to ^{5}P in collisions with argon. In Fig. 9 rate constants used in the current study are compared to those used in Li *et al.*'s initial interpretation of the experimental data. The current HP-CIE rate constant is approximately four orders of magnitude lower than the rate constant used by Li *et al.*, in large part because the strong collisional coupling of O(^{5}S$^\circ$) to O(^{5}P) is accomplished via collisions with electrons in the present model. Electron collisions are effective at coupling the two states because of the high electron translational temperature and an E-CIE rate that is approximately 400 times larger than that used by Li *et al.* The large discrepancy in the O(^{5}S$^\circ$ → ^{3}P) E-CIE rate is caused by assuming that the effective collision strengths of the O(^{3}P →^{5} S^o) and O(^{5}S$^\circ$ → ^{5}P) excitation reactions are the same; in reality, the above-threshold E-CIE cross sections for O(^{5}S$^\circ$ → ^{5}P) are two orders of magnitude higher than those for O(^{3}P →^{5} S^o).

The predicted number densities of O(^{5}S$^\circ$) and O(^{5}P) are compared with the measured data from the Li-21-2 experiment in Fig. 10. The model successfully reproduces the observed three-stage behavior observed in the experimental data, matching quantitatively within 10-20% for $n_{O(^5S^\circ)}$ and within 30% for all but the last data point of $n_{O(^5P_3)}$. Across all of the Li-21 experiments, the agreement with $n_{O(^5S^\circ)}$ and $n_{O(^5P_3)}$ is similar to that shown in Fig. 10, with model predictions overshooting the late-time measured number densities of O(^{5}P$_3$) by a maximum of 65% and O(^{5}S$^\circ$) number densities disagreeing with the measured data by a maximum of 33%.

All previous studies have analyzed the multistage behavior observed in Fig. 10 using simplified collisional-radiative models involving only the ground and measured electronic states [9–11]. In those models, the multistage behavior is explained as follows. First, the population of O(^{5}S$^\circ$) rises in Region I due to heavy particle impact excitation of O(^{3}P) in collisions with argon. Note the use of Roman numerals to distinguish these time history regions from the shock tube flow regions. Next, the measured population decreases in Region II as the translationally cold electrons scatter superelastically in collisions that de-excite O(^{5}S$^\circ$) to O(^{3}P), raising the free-electron temperature in the process. Finally, in Region III, the free-electron translational temperature surpasses $T_{ex,O(1,4)}$ and the population of O(^{5}S$^\circ$) begins rising again due to electron-impact excitation from O(^{3}P).

The current model also reproduces the experimentally observed three-stage behavior in the O(^{5}S$^\circ$) number density time history; however, the driving mechanisms in Regions II and III are distinct from those previously proposed in [9–11]. In Region I, the previous and current models agree that the excited state number density increase is due to heavy-particle excitation processes. Predictions begin to differ in Region II, with the present model predicting T_{eex} to be almost fully relaxed, in contrast to previous models in which T_{eex} is not fully relaxed until the end of the test time. Because T_{eex} ex-

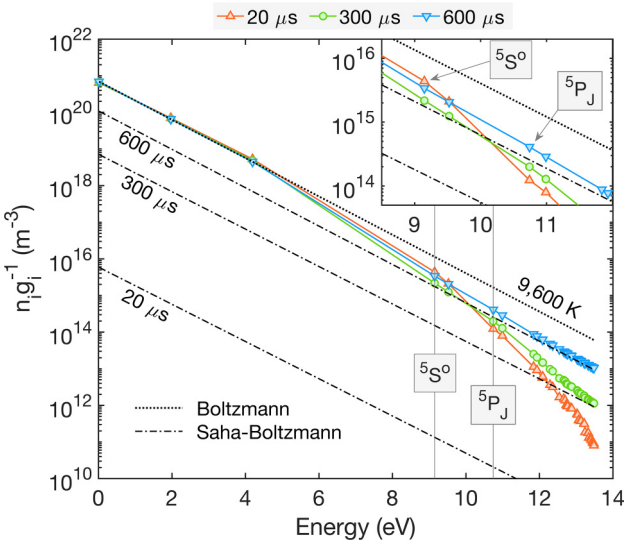

FIG. 11. Boltzmann plot showing the electronic state distribution of oxygen atoms at three different time points in the Li-21-2 experiment.

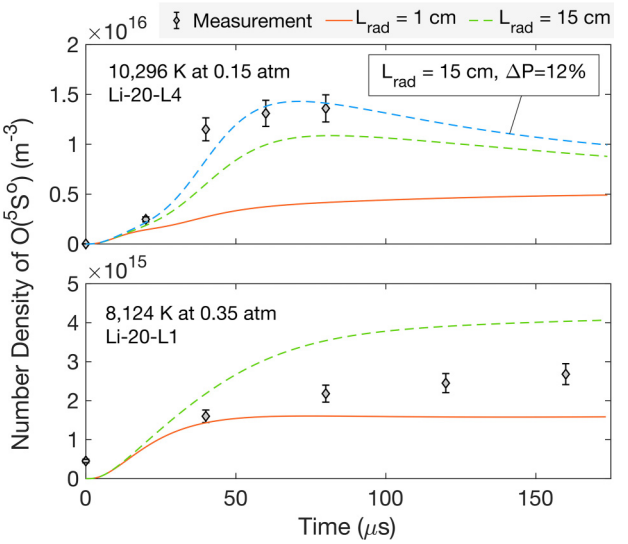

FIG. 12. Comparison between measured data and model predictions for the number density of $O(^5S^\circ)$ in the Li-20-L1 and Li-20-L4 experiments.

ceeds $T_{ex,O(i\leqslant 3,4)}$ after the first 20 μs of the experiment, the de-excitation of $O(^5S^\circ)$ via electron collisions cannot occur. Rather, the present model predicts that $O(^5S^\circ)$ depopulates in Region II as a result of ladder climbing to upper states that are subsequently ionized by the translationally hot free electrons. The high-lying electronic states, including the measured states, remain suppressed until the electron population approaches equilibrium, at which point the state populations begin rising again (Region III) to a Boltzmann population at the equilibrium temperature.

A Boltzmann plot of the electronic states of atomic oxygen is shown in Fig. 11 that clearly illustrates the mechanisms driving the three-stage behavior. Three key time points in the Li-21-2 experiment are shown: 20 μs, the transition point from Region I to Region II; 300 μs, the transition point from Region II to Region III; and 600 μs, the end of the simulation and well into Region III. At all three time points, the metastable ^1D and ^1S states are in equilibrium with the translational temperatures of the free electrons and heavy particles, meaning that the observed dynamics are indicative of only the upper-state kinetics.

At 20 μs, the $O(^5S^\circ)$ state has been driven close to equilibrium with T_{tr}, but the electron number density and temperature have just reached the critical value at which electron impact ionization begins to dominate the kinetics, and the upper electronic state populations begin falling as they are pulled toward the Saha-Boltzmann equilibrium line. At 300 μs, the highest-lying electronic states achieve Saha-Boltzmann equilibrium with the rising free-electron number density. From 300 μs to the third sampled time point at 600 μs, the upper states remain in Saha-Boltzmann equilibrium with the rising electron number density, raising their population and leading to the observed Region III population increase.

The modeled three-stage dynamics rely on the inclusion of states both below and above the measured $O(^5S^\circ)$ level. The metastable states drive the fast relaxation of the free electron temperature, and the upper states are required to resolve the ladder-climbing behavior of electron impact ionization [35].

Kinetics in the Li-21 experiments are primarily driven by electron-impact processes. The excellent predictions obtained across the Li-21 experiments indicate that the collisional-radiative model effectively predicts electron temperature relaxation, E-CIE, and E-CII at the studied conditions. Heavy particle kinetics can be better assessed through the analysis of experiments at lower pressure and/or temperature, as in the Li-20 data set, or with increased time resolution, as in the Minesi data set.

Predictions of $O(^5S^\circ)$ are compared with experimental measurements from the Li-20-L1 and Li-20-L4 experiments in Fig. 12. The model produces reasonable predictions for the Li-20-L1 case but underpredicts the Li-20-L4 measurements by up to 80%. The excitation of $O(^5S^\circ)$ appears to follow a temperature dependence based on a threshold energy that is approximately 40% greater than the $O(^3P \rightarrow {}^5S^\circ)$ excitation energy, in line with the findings of Minesi *et al.* [11]. Reaction thresholds do not need to exactly match the energetic difference between the two involved states; however, such a large deviation appears improbable. Radiation modeling and nonideal pressure rise may also play a role in explaining the observed temperature dependence.

Escape factor calculations require a length scale, L_{rad}, over which the absorption takes place, and there is some ambiguity in the choice of this length scale. Two reasonable choices for the present analyses are the shock tube diameter and the characteristic length scale of flow gradients. Ambiguity in the choice of L_{rad} is introduced by the three-dimensionality of radiation transport: the shock tube diameter is the relevant length scale for absorption in the radial direction and the gradient length scale is relevant for absorption along the axial direction of the shock tube. In Fig. 12 the choice between the two values of L_{rad} is shown to strongly influence the predicted time histories in the low-pressure Li-20 experiments. For the Li-20-L1 experiment, the experimental data are bracketed by

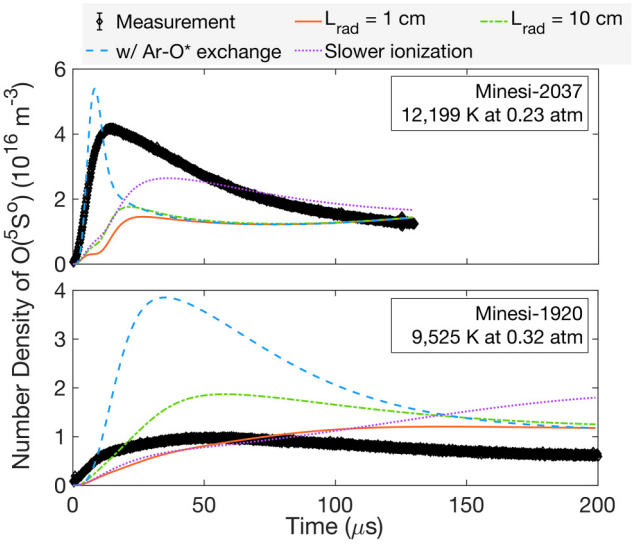

FIG. 13. Comparison between model predictions and measured data for the number density of $O(^5S^\circ)$ in the Minesi-1920 and Minesi-2037 experiments.

predictions from the two values of L_{rad}. In both cases, predictions when $L_{\text{rad}} = D_{\text{shock tube}} = 15$ cm are very close to those where Λ_{51} is set to zero; i.e., when emission due to the $O(^3S^\circ \rightarrow {}^3P)$ transition is fully self-absorbed as is often assumed for vacuum ultraviolet (VUV) resonance radiation [102]. The choice of $L_{\text{rad}} = 1$ cm results in a partial escape of $O(^3S^\circ \rightarrow {}^3P)$ radiation that is consistent with the observed suppression of $O(^3S^\circ)$ populations relative to $O(^5S^\circ)$ in the Nations-16 data.

The true physics of resonance radiation transport cannot be fully accounted for within the present model because escape factors assume local absorption. If the $O(^3S^\circ \rightarrow {}^3P)$ emission partially escapes the local fluid element into the upstream and/or downstream flow directions, as the $L_{\text{rad}} = 1$ cm escape factors indicate, then the emitted light is absorbed elsewhere and influences the measured populations at those locations.

Nonideal pressure rise may also contribute to the observed temperature dependence. The effect of a dP/dt corresponding to 12% net pressure increase is shown in Fig. 12 for the Li-20-L4 case. The incorporation of nonideal pressure rise results in a faster excitation of the measured state. In shock tube experiments, higher temperatures are typically accompanied by lower pressures, where nonideal effects are more significant. Because nonideal pressure rises are not reported in the Li-20 experiments, it is not possible to test this hypothesis. Future measurements of excited state and electron number densities should report the measured dP/dt in each experiment.

Measurements from Minesi *et al.* [11] with a time resolution of 0.2 μs provide another valuable probe of excited state kinetics under the primary influence of excitation by heavy particles. Collisional-radiative model predictions are compared against two experiments from the Minesi data set in Fig. 13. For these experiments, the baseline model with $L_{\text{rad}} = 1$ cm obtains only order-of-magnitude agreement with the measured data, with differences exceeding a factor of 3 in some cases.

There are several possibilities for the disagreements between the collisional-radiative model predictions and the Minesi data. While predictions of the Minesi-1920 experiment are sensitive to the choice of radiation length scale, those of the Minesi-2037 experiment are not strongly influenced by the choice of L_{rad}. Radiation modeling uncertainties may play a role in, but cannot completely explain, the largest discrepancies. Another important feature of the Minesi experiments is the relatively large nonideal pressure rise compared to the other analyzed experiments. If the nonideal pressure rise is not fully isentropic, then $dh = \nu dp$ will overpredict the enthalpy increase, potentially explaining the long-time overprediction of $O(^5S^\circ)$ populations in the Minesi-1920 experiment.

Recalling the previous explanation for the three-stage behavior in the Li-21 experiments, the higher maximum number density of $O(^5S^\circ)$ could be caused by slower ionization: a slower buildup of electrons would delay the onset of Region II depletion via electron impact ionization, allowing the excited state concentration to rise for longer before the onset of significant electron impact ionization. A model with slower ionization is obtained by scaling the excitation rate constants for $\text{Ar}(1) + \text{Ar} \rightarrow \text{Ar}(i) + \text{Ar}$ by a factor of 1/5, matching those of Kelly [94]. The maximum number density of $O(^5S^\circ)$ is increased when the slower ionization rate is adopted. Continued reduction of the ionization rate leads to progressively higher peak number densities; however, the timescale of the $O(^5S^\circ)$ population rise remains significantly slower than the measured data suggest.

One process that produces $O(^5S^\circ)$ on the timescale observed in the Minesi-2037 experiment is the electronic excitation exchange between the $4s$ states of argon and the $3p^3P$ state of atomic oxygen, modeled using the room temperature rate measured by Piper [58]. In general, however, including this process worsens the agreement between model predictions and measurements for most cases analyzed, the Minesi-1920 case being one such example. Measurements of metastable argon atoms, which absorb in the infrared, would clarify the potential effect of electronic exchange between excited argon and oxygen atoms.

The underprediction of $O(^5S^\circ)$ number density measurements in the Minesi data set is contrasted by the overprediction of early-time $O(^5S^\circ)$ number density measurements in the high-pressure experiments performed by Li *et al.* [9]. An example is shown in Fig. 14 for the Li-20-H2 case, where the peak excited state number density is overestimated by a factor of two at very early times when $L_{\text{rad}} = 1$ cm. Such a result apparently contradicts the disagreement observed in the Minesi-1920 data taken at a similar translational temperature.

V. SENSITIVITY ANALYSIS

A major conclusion of the present study is that measured data for high-lying atomic electronic states behind strong shock waves must be interpreted using a more complete collisional-radiative model like the one developed in this work. One challenge when adopting such a model is that its predictions are the result of hundreds of different parameter choices, and it can be difficult to identify which processes most sensitively influence a given model prediction.

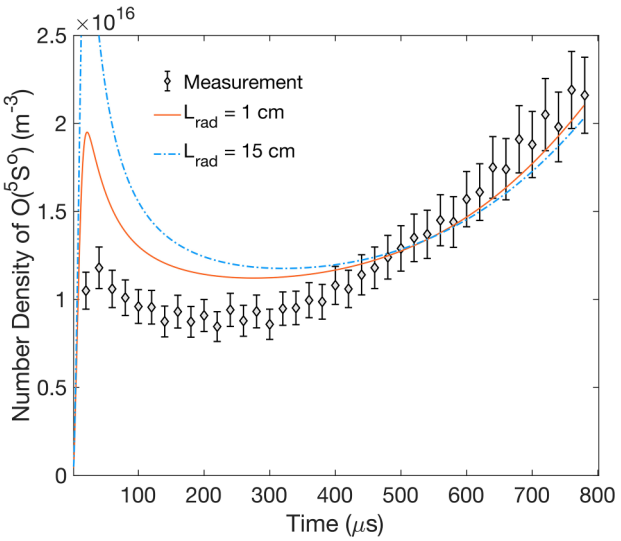

FIG. 14. Comparison between model predictions and measured data for the number density of $O(^5S^\circ)$ in the Li-20-H2 experiment at 9,161 K and 0.95 atm in 1% O_2-Ar.

Such ambiguity is resolved in the present section by means of a global sensitivity analysis that quantitatively apportions the variance in model predictions to variations in individual input parameters. The quantification of variance contributions from each individual parameter is accomplished using total Sobol' indices, a popular metric used in global sensitivity analyses.

The sensitivity analysis methods applied in the present work are adapted from those used in several studies by West *et al.* [103–105] to perform sensitivity analysis of multidimensional flowfield calculations with consideration of several hundred uncertain parameters. A full discussion of the sensitivity analysis technique and its implementation is provided in Appendix A.

A. Parameters and response functions

The quantities of interest in the sensitivity analysis are the number density of the species and electronic states that are probed in each experiment. The PCE surrogate is fit to the logarithm of the number density instead of the number density itself, improving both the convergence of the Sobol' indices and the accuracy of the surrogate model. Response functions are extracted for each quantity of interest at a set of 75 logarithmically spaced time points from 0.5 μs to the end of the test time.

A total of 295 parameters are included in the sensitivity analysis. The parameters include rate coefficients for collisionally induced electronic transitions:

(1) Among the lowest ten states of O in collisions with electrons and argon atoms

(2) From ground-state argon to the radiatively coupled excited states in collisions with other argon atoms

(3) From ground-state argon to all higher levels by electron collisions

(4) Among the lowest five levels of argon by electron and Ar collisions

(5) Among the electronic states of O_2 in collisions with O_2, O, Ar, and electrons

(6) And between the two excited states of Ar^+ by electron collisions.

Rate coefficients for ionization by impact with electrons and argon atoms are included for the lowest ten levels of O, all electronic levels of O_2, and the lowest five levels of Ar. All rate coefficients for quenching, electronic excitation exchange and energy pooling, dissociation, charge exchange, and associative ionization are also considered.

Relaxation parameters are considered as well, including the vibrational-translational relaxation times for O_2 with Ar, O, and O_2 and the energy exchange cross sections between electrons and all six heavy species. Finally, the escape factors for radiative transitions among the lowest ten states of oxygen are included.

The value of each parameter is varied over a log-uniform distribution, with minimum and maximum values obtained by multiplying the parameter's value in the baseline model by 0.1 and 10, respectively. Note that, in the case of Ar + Ar electronic excitation, the adopted rate coefficient is 55 times larger than the lowest value published in the literature, as shown in Fig. 6. However, this lowest rate coefficient from the literature yields predictions that are highly inconsistent with the analyzed electron number density measurements. Thus, a one-order-of-magnitude variation is deemed a sufficient variation of the Ar + Ar excitation rate coefficients.

Another class of rate coefficient uncertainties worth addressing is those of the HP-CIE reactions of oxygen with argon. Analytical expressions have been published in the literature that predict HP-CIE reactions as much as four orders of magnitude larger than those adopted in the present model. This large variation among rate coefficient sources is neglected when constructing uncertainty intervals for HP-CIE reactions because such large values of the excitation rate coefficients yield predictions that are highly inconsistent with the analyzed atomic oxygen excited state data. Given the overall agreement between the present model and the data analyzed in Sec. IV D at conditions where HP-CIE is important, an order-of-magnitude variation to the adopted HP-CIE rate coefficients is considered an appropriate representation of the potential variation in Ar + O HP-CIE rate coefficients.

B. Results

Sensitivity analysis is performed for all of the experimental conditions in Table IX where electronically excited oxygen atoms were measured. Results from three cases are shown in this section that together demonstrate the full diversity of sensitivity results observed across all analyzed conditions. The Sobol' index convergence results are presented and discussed in Appendix B.

Sobol' indices for the number density of $O(^5S^\circ)$ and $O(^3S^\circ)$ in the Nations-16 case are plotted in Fig. 15. The escape factor for 130 nm radiative emission from the $O(^3S^\circ \rightarrow {}^3P)$ transition, Λ_{51}, dominates the sensitivity of $O(^3S^\circ)$ and plays a leading role in the $O(^5S^\circ)$ time history as well. In the case of $O(^3S^\circ)$, the dominance of Λ_{51} highlights the difficulty of assessing the rates of collisional excitation processes using the measured time history. The situation with $O(^5S^\circ)$ is somewhat

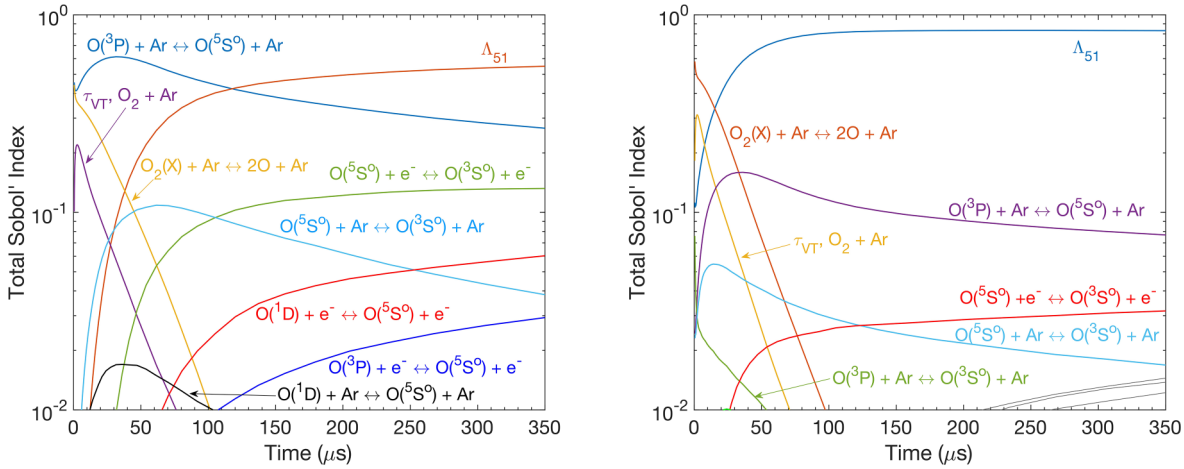

(a) $O(^5S^\circ)$ (b) $O(^3S^\circ)$

FIG. 15. Total Sobol' indices for the number density of (a) $O(^5S^\circ)$ and (b) $O(^3S^\circ)$ in the Nations-16 experiment at 7,250 K and 0.61 atm in 1% O_2-Ar.

better, with the HP-CIE of $O(^5S^\circ)$ from $O(^3P)$ showing major sensitivity, indicating that rate inferences are appropriate using this time history.

The sensitivity of Λ_{51} indicates that radiative loss is a major contributor to the population of $O(^3S^\circ)$ in the Nations-16 case, consistent with the suppressed $T_{ex,O(4,5)}$ calculated using the measured data. Collisional excitation between the two states is also shown to be important in Fig. 15, likely because the two states are far from equilibrium and separated by a small energy gap. Modeling of $O(^5S^\circ)$ populations should therefore take into account the collisional excitation to and radiative loss from the $O(^3S^\circ)$ state.

The final processes worth noting from the Nations-16 sensitivities are the vibrational-translational relaxation between O_2 and Ar and the dissociation of $O_2(X)$ by Ar. Vibrational relaxation is important because it defines the time history of T_{vib}, which in turn influences the nonequilibrium rate of dissociation. Dissociation and vibrational relaxation are only sensitive early in the test, after which the dissociation fraction of O_2 is near equilibrium. Similar short timescales for the sensitivity of these two processes are found across all conditions analyzed.

Electron number density sensitivities are plotted in Fig. 16 for the Li-21-1 case. The most important process, by far, is the excitation of argon from its ground state to its third and fifth excited states, consistent with previous discussions on the ionization mechanism in shocked argon and the analysis in [24]. Electron impact processes rise in sensitivity over time; however, the test time ends before the electron concentration reaches a sufficient level for electron impact ionization to dominate. The excitation of $O(^1D)$ by electron and argon atom impact is also important due to the role of $O(^1D)$ in mediating energy exchange between the heavy particles and the free electrons.

The number of sensitive processes influencing the concentrations of $O(^5S^\circ)$ and $O(^5P)$ is far greater than the number of processes influencing the electron concentration. To clarify the relative contributions of each process to the overall solution variance, the Sobol' indices are plotted in Fig. 17 after being normalized so that they sum to one. The top 12 processes influencing each time history are labeled individually, with the summed contribution from the remaining 283 processes shown in gray at the top of each plot. The processes influencing each measured state are very similar, indicating that the coupling between the two states is strong.

Early in both time histories, the heavy particle impact excitation of $O(^3P)$ to $O(^5S^\circ)$ dominates the sensitivity along with the dissociation of $O_2(X)$ by argon. The escape factor for the radiative transition between the two measured states is also important, particularly for the ^5P number density, although the contribution is short-lived.

Similar electron impact excitation reactions play a dominant role in the sensitivity of both electronic state number densities. Excitation of $O(^5S^\circ)$ from the metastable ^1D level is

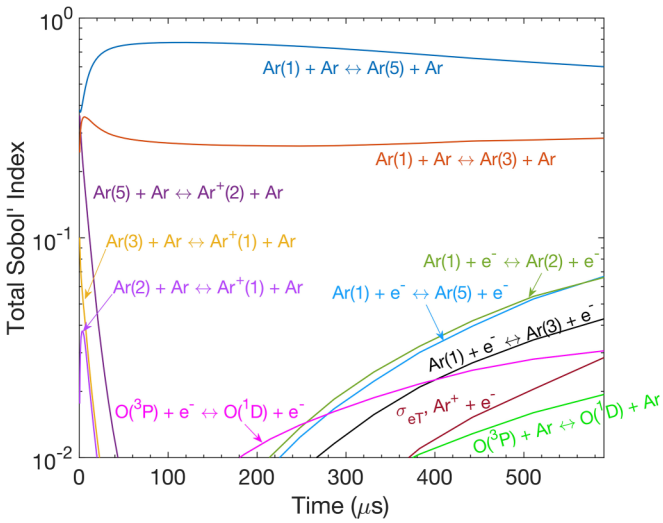

FIG. 16. Total Sobol' indices for the prediction of electron number density in the Li-21-1 case at 10,153 K and 0.49 atm in 1% O_2-Ar.

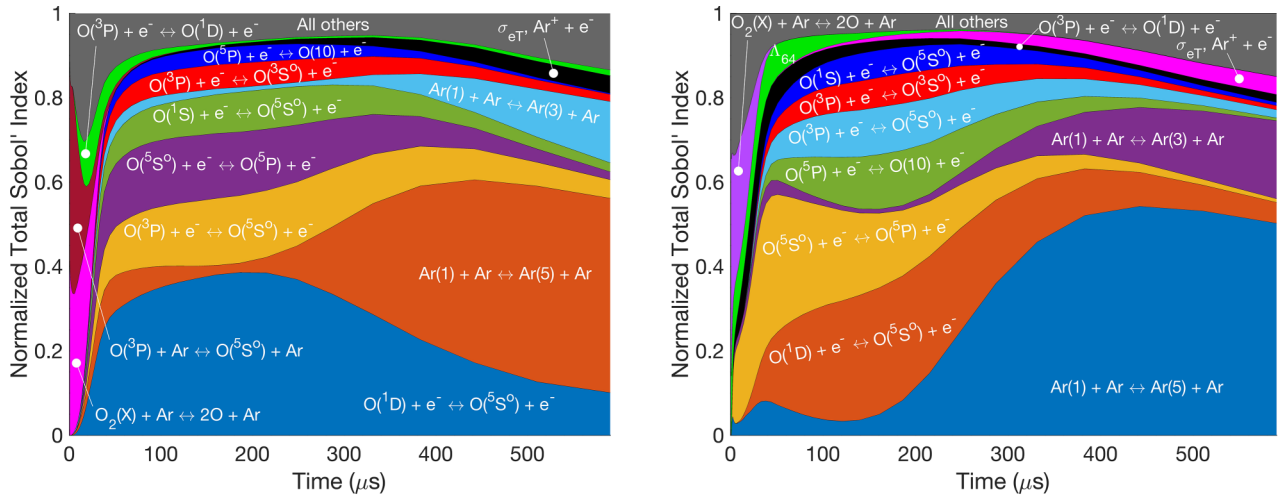

(a) $O(^5S^\circ)$ (b) $O(^5P)$

FIG. 17. Normalized total Sobol' indices for the number density of (a) $O(^5S^\circ)$ and (b) $O(^5P)$ in the Li-21-1 experiment at 10,153 K and 0.49 atm in 1% O_2-Ar.

significantly more sensitive than excitation from the ground, indicating that ladder-hopping to the measured state must be considered when analyzing measured time histories of $O(^5S^\circ)$ and $O(^5P)$. Excitation between the two measured states is also highly sensitive because it defines the balance of collisional and radiative coupling between the two states. The E-CIE reaction from the ^5P state to the tenth excited state of O is sensitive for the same reason. Formation of the $^3S^\circ$ state remains sensitive as in the Nations-16 case. The late-time sensitivities in Fig. 17 are dominated by processes that influence the overall system dynamics, highlighting the ability of these high-lying states to probe the timescale of ionization in the gas.

Finally, the normalized Sobol' indices for the Minesi-2037 experiment are shown in Fig. 18. The included processes and the timescales over which they are important are similar to the Li-21-1 experiment. In spite of the similarity in sensitive processes between both experiments, the model predictions are only consistent with the measured data from the Li-21 experiments and not from the Minesi experiments. In light of this observation, more data are needed to help identify aspects of the flow, radiation, or kinetics modeling that may explain the discrepancies.

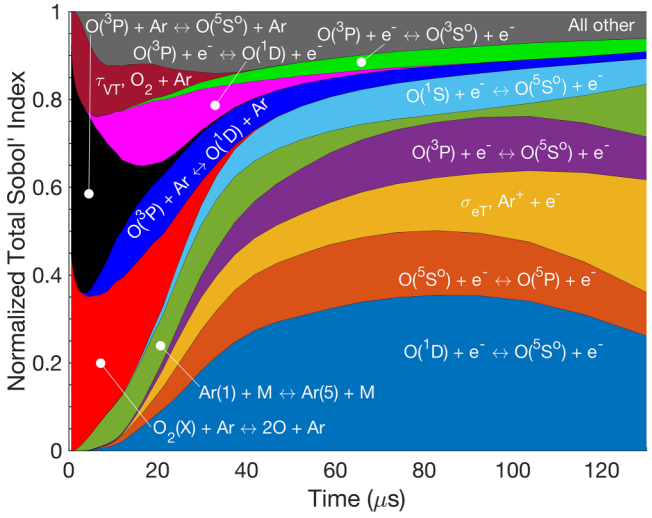

FIG. 18. Normalized total Sobol' indices for the number density of $O(^5S^\circ)$ in the Minesi-2037 experiment at 12 199 K and 0.23 atm in 1% O_2-Ar.

There are three quantities that, if measured, could enhance the development of the present collisional-radiative model and improve the utility of the excited state measurements analyzed in this work. First, electron number density measurements would be extremely valuable, especially in the same facility where the Minesi data were measured. Next, argon electronic state population measurements would elucidate whether the ionization rate is significantly affected by impurities and whether excitation exchange between oxygen and argon is an important process. Finally, measurements of $O(^1D)$, while challenging, would shed light on the proposed role of this metastable state in facilitating rapid energy exchange from the translational energy of heavy particles to the free electrons.

VI. CONCLUSION

In this paper, the electronic excitation and ionization kinetics occurring in oxygen-argon reflected shock experiments were analyzed using a three-temperature collisional-radiative model coupled to a one-dimensional inviscid flow solver. A thorough description of the governing equations and nonequilibrium energy exchange modeling was provided, and the selected parameters for each elementary process in the collisional-radiative model were described.

Model predictions were compared with experimental measurements for the number density of molecular oxygen, electrons, and three electronic states of atomic oxygen. Predictions for the dissociation of O_2 were consistent with the available data, ensuring that dissociation was predicted with

sufficient accuracy to study the measurements of excited atoms in conditions where dissociation was ongoing. Rate coefficients for the heavy particle impact excitation of argon, which determine the net ionization rate in the analyzed experiments, were inferred using comparison with electron number density measurements at 10 000 to 11 200 K. The inferred rate constant was higher than other published values, potentially due to impurities or pressure nonidealities behind the reflected shock. It is recommended that further measurements of electron number density across wider ranges of temperature and pressure be performed to help clarify the reasons for the observed ionization rate.

Next, the excited state number density measurements were analyzed using the collisional-radiative model. Excited state measurements at 7000 K were used to infer a rate constant for the excitation of $O(^3P)$ to $O(^5S^\circ)$ in collisions with argon. Multistage behavior, observed in several experiments, was also predicted by the collisional-radiative model, and a detailed explanation for it was given. The reason for the multistage behavior was different from previously proposed mechanisms, underscoring the value of analyzing the measured data using a more complete model. Future interpretations of atomic excited state measurements should adopt sufficiently detailed models capable of simulating these key mechanisms.

Nonideal pressure rises were incorporated into the governing equations when data were available, and their effect on the excited state population predictions was significant in several cases. It is recommended that nonideal pressure rise be reported alongside measured data for electron and excited atomic state populations in future reflected shock experiments. Parameters describing the reabsorption of resonance radiation were also found to play a major role in the excited state predictions, presenting a challenge for the model assessment due to the uncertainties inherent in the use of escape factors to model self-absorption.

The atomic excited state data came from shock tubes at Stanford and at UCLA. Model predictions were generally consistent with the Stanford data across a wide range of temperatures and pressures, with discrepancies typically being bounded by reasonable limits on the nonideal pressure rise and escape factor self-absorption length scale. When comparing with the data measured at UCLA, which has considerably higher time resolution than the Stanford data, major discrepancies between the model and experiment were observed. Several potential explanations were provided for the disagreement, but more data from the UCLA shock tube is necessary to identify whether facility effects or kinetic modeling inaccuracies are to blame; electron number density measurements would be particularly revealing.

Finally, a sensitivity analysis was performed to determine the rate coefficients and relaxation parameters that most influenced the electron and atomic excited state number densities. Predictions of the $O(^3S^\circ)$ population were primarily dependent on the escape factor for radiative de-excitation from $O(^3S^\circ)$ to $O(^3P)$. Rate coefficients coupling the three measured states were sensitive across all experimental conditions. In general, each excited state number density was influenced by collisionally induced excitation involving multiple lower and upper states, highlighting the necessity of adopting a detailed modeling approach to analyze the measured data, as well as the difficulty of inferring individual rate coefficients from the measurements.

Additional data from mixtures of O_2-Ar with higher concentrations of O_2 will help to expand the kinetic model validation to excitation processes that do not involve collisions with argon, which are particularly relevant for air plasmas. However, to effectively separate the effect of HP-CIE processes that do not involve argon, an accurate model of the argon-dominated kinetics must first be established. The present study has presented such a model, providing a foundation for future studies of oxygen excitation kinetics in mixtures with higher concentrations of oxygen in argon.

ACKNOWLEDGMENTS

The authors thank Dr. Yang Li, Dr. Jesse W. Streicher, Dr. Nicolas Q. Minesi, and Dr. Kyle M. Hanquist for providing the data that was analyzed in this work. The authors' understanding of the data and experimental methods was greatly enhanced through conversations with Dr. Li, Dr. Streicher, and Dr. Minesi. Numerous productive discussions with and useful feedback from Dr. Ross S. Chaudhry, Dr. Peter M. Finch, Dr. Ajay Krish, and Dr. Kyle M. Hanquist have also contributed to the quality of this work. We are grateful to Dr. Thomas K. West and Nick Carter for valuable discussions about sparse point-collocation sensitivity analysis techniques. The authors would also like to thank Dr. Klaus Bartschat for providing the B-Spline R-Matrix calculation results for O and Ar. This work was supported by the U.S. Air Force Office of Scientific Research Grant No. FA9550-21-1-0075 and the Office of Naval Research MURI Grant No. N00014-22-1-2661. This work utilized the Blanca condo computing resource at the University of Colorado Boulder. Blanca is jointly funded by computing users and the University of Colorado Boulder.

APPENDIX A: SENSITIVITY ANALYSIS METHODOLOGY

a. Polynomial chaos expansions

The adopted sensitivity analysis technique relies on the construction of a polynomial chaos expansion surrogate model to approximate the collisional-radiative model predictions. The surrogate model is given by the sum of orthogonal polynomial basis functions shown in Eq. (A1) that approximate the mapping between uncertain parameter values and a given quantity of interest (QoI), also referred to as the response function. The PCE surrogate is defined as

$$\hat{R} = \sum_{j=0}^{N_P} \alpha_j \Psi_j(\boldsymbol{\xi}), \tag{A1}$$

where $\hat{R}$ is the approximated response function value, N_P is the number of polynomial basis functions, Ψ_j are the basis functions, α_j are the basis function coefficients, and $\boldsymbol{\xi}$ is the vector of uncertain parameters that have been normalized to the interval $[-1,1]$. Polynomial chaos expansions are ideal because statistical quantities such as partial variances and the total variance can be calculated directly from the PCE basis coefficients, α_j, enabling a computationally efficient determination of Sobol' indices [106].

Computation of the total Sobol' indices using the PCE coefficient vector, $\boldsymbol{\alpha}$, is performed using Eq. (A2),

$$S_{T,i} = \sum_{\mathbf{k}\in\mathcal{A}_i} \alpha_{\mathbf{k}}^2 / D, \quad \mathcal{A}_i = \{\mathbf{k} \in \mathcal{A} : k_i \neq 0\}, \tag{A2}$$

where $\mathcal{A}$ is the set of multi-indices $\mathbf{k} = (k_1, \ldots, k_{N_\xi})$, for each polynomial basis function that identifies which of the N_ξ normalized uncertain parameters, ξ_i, that each polynomial depends upon.

The approximated total variance, $\hat{D}$, is calculated using the PCE surrogate weighting coefficients using

$$\hat{D} = \sum_{j=1}^{N_P} \alpha_j^2. \tag{A3}$$

The $j = 0$ polynomial does not contribute to the variance because Ψ_0 is a constant that is equal to the mean of the approximated response function $\hat{R}$.

b. Point-collocation with sparse approximation

Basis coefficients of the PCE surrogate are determined using a nonintrusive point collocation technique as in [103–105]. In this approach, the collisional-radiative model is evaluated at a set of sample points, and the sampled response function values are used to construct the following linear system:

$$\begin{pmatrix} R(\boldsymbol{\xi}_1) \\ R(\boldsymbol{\xi}_2) \\ \vdots \\ R(\boldsymbol{\xi}_{N_s}) \end{pmatrix} = \begin{pmatrix} \Psi_0(\boldsymbol{\xi}_1) & \Psi_1(\boldsymbol{\xi}_1) & \cdots & \Psi_{N_P}(\boldsymbol{\xi}_1) \\ \Psi_0(\boldsymbol{\xi}_2) & \Psi_1(\boldsymbol{\xi}_2) & \cdots & \Psi_{N_P}(\boldsymbol{\xi}_2) \\ \vdots & \vdots & \ddots & \vdots \\ \Psi_0(\boldsymbol{\xi}_{N_s}) & \Psi_1(\boldsymbol{\xi}_{N_s}) & \cdots & \Psi_{N_P}(\boldsymbol{\xi}_{N_s}) \end{pmatrix} \begin{pmatrix} \alpha_0 \\ \alpha_1 \\ \vdots \\ \alpha_{N_P} \end{pmatrix}. \tag{A4}$$

The matrix in Eq. (A4), $\boldsymbol{\Psi}$, also known as the measurement matrix, contains the basis polynomials evaluated at the sampled parameter values $\boldsymbol{\xi}$, where the subscripts are sample indices. The number of samples is denoted as N_s. The response function returned by the collisional-radiative model for a given sample is denoted as $R(\boldsymbol{\xi})$.

The solution of Eq. (A4) is fully determined when the number of samples matches the number of basis polynomials. In this study, a second-order PCE surrogate is employed to consider 295 uncertain parameters, leading to an expansion consisting of 43 956 polynomials. Such a large number of collisional-radiative model evaluations is very computationally demanding, motivating the adoption of a solution technique for the case where $N_s \ll N_P$.

Equation (A4) is underdetermined when $N_s < N_P$, so a regularization constraint is required to specify a unique solution. Following [103–105], an L_1 regularization constraint is added to Eq. (A4), yielding Eq. (A5), which has a unique solution when δ, the tolerance, is set to zero [104].:

$$\min \|\boldsymbol{\alpha}\|_1 \text{ subject to } \|\boldsymbol{\Psi}\boldsymbol{\alpha} - \boldsymbol{R}\| < \delta. \tag{A5}$$

Regularization using an L_1 constraint is a common technique in sensitivity analysis when it is not feasible to evaluate the deterministic model N_P times [107]. Minimization of the L_1 norm is an effective technique for achieving solution vectors, $\boldsymbol{\alpha}$, with the minimum number of nonzero values.

c. Solution algorithm and implementation

While Eq. (A5) can be solved with any number of samples, the solutions with an extremely small N_s are unlikely to accurately represent the true system behavior. To address this, Eq. (A5) is solved with incrementally increasing values of N_s, and the changes to the Sobol' indices determined from the resulting expansion are monitored to assess the convergence of the solution.

Samples for the uncertain parameters are drawn from a joint-uniform distribution made up of N_ξ uniform marginal distributions, each one corresponding to a separate parameter. The values of each parameter are sampled over a given range that is then transformed into logarithmic space and normalized to the interval [−1,1]; this interval defines the endpoints of each marginal distribution.

A Latin hypercube of N_P samples is then generated from the resulting joint-uniform distribution. Latin hypercube sampling is preferred over Monte Carlo sampling because it provides better sample space coverage when the number of samples is low [104]. Next, orthonormal Legendre polynomials are constructed on the joint-uniform distribution. The Python library `chaospy` is used to manage the joint and marginal distributions, as well as the Latin hypercube parameter sampling [108]. A custom `Polynomial` class is constructed to efficiently generate and evaluate the Legendre polynomials.

After constructing the joint distribution, sample set, and orthonormal polynomials, the sensitivity analysis algorithm proceeds as follows:

(1) Evaluate the collisional-radiative model for a batch of 40 samples extracted from the full Latin hypercube sample set.

(2) Extract the response function values at the evaluated sample points.

(3) Solve Eq. (A5) for the expansion coefficients of each response function PCE.

(4) Calculate Sobol' indices from the expansion coefficients using Eq. (A2).

(5) Evaluate 40 more samples from the initial Latin hypercube sample set.

(6) Solve Eq. (A5) for the expansion coefficients of each response function PCE.

(7) Evaluate convergence metrics.

(8) Repeat steps 5–7 until the maximum number of samples is reached.

Batches of 40 samples are run in parallel using `GNU Parallel` [109]. Equation (A5) is solved using the `spgl1` Python package [110,111], and the `spgl1` solutions are also performed in parallel, again using `GNU Parallel`.

d. Convergence metrics

Convergence of the PCE surrogate is quantified using two metrics. The first metric tracks the maximum and average shifts in the Sobol' indices with the introduction of each new sample batch, considering all response functions. These metrics are defined as

$$|\Delta S_T|_{\max,b} = \max\{\text{abs}(S_{T,i,b} - S_{T,i,b-1})_R \mid i \in [1..n] \text{ and } R \in \mathcal{R}\}, \tag{A6}$$

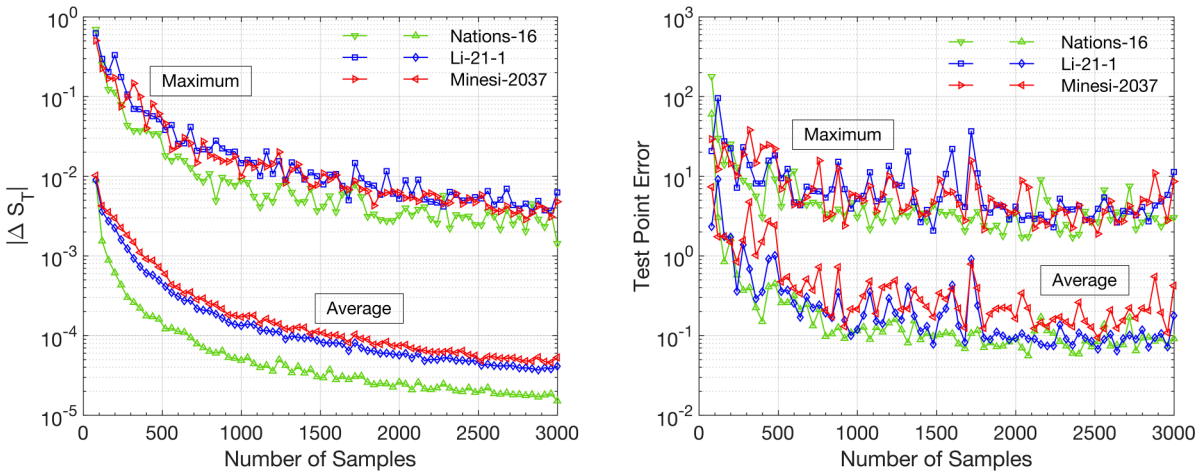

(a) Change in Sobol' indices (b) Surrogate model test point error

FIG. 19. Convergence metrics for the sensitivity analyses.

$$|\Delta S_T|_{\text{avg},b} = \text{mean}\{\text{abs}(S_{T,i,b} - S_{T,i,b-1})_R \mid i \in [1..n] \text{ and } R \in \mathcal{R}\}, \tag{A7}$$

where $\mathcal{R}$ is the set of all response functions, i is the parameter index, and b indicates the number of sample batches incorporated in solving Eq. (A5) to obtain $S_{T,i,b}$.

The second metric quantifies the difference between the response function that is approximated by the PCE surrogate, $\hat{R}$, and the true response function values returned by the collisional-radiative model, R. Because the surrogate accurately predicts the response function values that inform the selection of its coefficients via Eq. (A5), the points used to fit the surrogate model are not useful for assessing its accuracy; additional "test point" samples are needed.

To avoid evaluating the collisional-radiative model for the sole purpose of surrogate accuracy quantification, the R returned by the collisional-radiative model for the samples in the bth batch are compared with the $\hat{R}$ predicted by the surrogate model that was fitted using $b-1$ sample batches. Mathematically, this is expressed as

$$T_{\max,b} = \max\{\text{abs}[R(\xi_s) - \hat{R}_{b-1}(\xi_s)] \mid s \in \mathcal{B}_b \text{ and } R \in \mathcal{R}\}, \tag{A8}$$

$$T_{\text{avg},b} = \text{mean}\{\text{abs}[R(\xi_s) - \hat{R}_{b-1}(\xi_s)] \mid s \in \mathcal{B}_b \text{ and } R \in \mathcal{R}\}, \tag{A9}$$

where T is the test point error, s are sample indices, $\mathcal{B}_b$ is the set of sample indices from batch b, and $\hat{R}_{b-1}$ is the surrogate model fitted using $b-1$ sample batches.

APPENDIX B: CONVERGENCE OF SOBOL' INDICES

Convergence metrics for the three analyzed conditions are plotted in Fig. 19. After evaluating the collisional-radiative model 3000 times for each condition, the maximum change to any Sobol' index drops well below 0.01 for all three cases as shown in Fig. 19(a). The average change in Sobol' indices is considerably lower, brought down by the large number of Sobol' indices close to zero. The PCE surrogate test point error is plotted in Fig. 19(b). Test point error is reported for the number density, not its logarithm, to provide a clearer picture of the surrogate model performance. Although the maximum errors are between 300% and 1000%, the average errors are between 6% and 30%, indicating that the maximum test point error occurs at only one or two of the 75 points in each profile. For the remaining points, the error must be closer to the average of approximately 10%, which is consistent with the test point errors observed by West and Hosder [104]. Due to the apparent locality of the maximum test point error and the excellent convergence of the total Sobol' indices, the fitted PCE surrogate is deemed acceptable.

[1] S. M. Jo, O. J. Kwon, and J. G. Kim, Electronic-state-resolved analysis of high-enthalpy air plasma flows, Phys. Rev. E **100**, 033203 (2019).

[2] R. S. Chaudhry and I. D. Boyd, Vehicle-scale simulations of hypersonic flows using the MMT chemical kinetics model, in *AIAA Aviation 2020 Forum* (American Institute of Aeronautics and Astronautics, Virtual Event, 2020).

[3] P. Sawicki, R. S. Chaudhry, and I. D. Boyd, Influence of chemical kinetics models on plasma generation in hypersonic flight, in *AIAA Scitech 2021 Forum* (American Institute of Aeronautics and Astronautics, Virtual Event, 2021).

[4] Q. Niu, Z. Yuan, B. Chen, and S. Dong, Infrared radiation characteristics of a hypersonic vehicle under time-varying angles of attack, Chinese J. Aeronaut. **32**, 861 (2019).

[5] C. Park, Review of chemical-kinetic problems of future NASA missions, I: Earth entries, J. Thermophys. Heat Transfer **7**, 385 (1993).

[6] R. S. Chaudhry and G. V. Candler, Statistical analyses of quasiclassical trajectory data for air dissociation, in *AIAA Scitech*

2019 Forum (American Institute of Aeronautics and Astronautics, San Diego, CA, 2019).

[7] I. D. Boyd and E. Josyula, Analysis of associative ionization rates for hypersonic flows, J. Thermophys. Heat Transfer **35**, 1 (2021).

[8] M. Nations, S. Wang, C. S. Goldenstein, D. F. Davidson, and R. K. Hanson, Kinetics of excited oxygen formation in shock-heated O_2-Ar mixtures, J. Phys. Chem. A **120**, 8234 (2016).

[9] Y. Li, S. Wang, C. L. Strand, and R. K. Hanson, Two-temperature Collisional-radiative modeling of partially ionized O_2-Ar mixtures over 8,000–10,000 K behind reflected shock waves, J. Phys. Chem. A **124**, 3687 (2020).

[10] Y. Li, Y. Wang, D. F. Davidson, and R. K. Hanson, Collisional excitation kinetics for $O(3s\,^5S^o)$ and $O(3p\,^5P_3)$ states using laser absorption spectroscopy in shock-heated weakly ionized O_2-Ar mixture, Phys. Rev. E **103**, 063211 (2021).

[11] N. Q. Minesi, A. P. Nair, M. O. Richmond, N. M. Kuenning, C. C. Jelloian, and R. M. Spearrin, Excited oxygen kinetics at electronvolt temperatures via 5-MHz RF-diplexed laser absorption spectroscopy, Appl. Opt. **62**, 782 (2023).

[12] T. T. Aiken and I. D. Boyd, Two-temperature modeling of nonequilibrium relaxation and dissociation in shock-heated oxygen, J. Thermophys. Heat Transfer **37**, 723 (2023).

[13] L. Presley and R. Hanson, Exact solutions of reflected normal shock-wave flow fields with nonequilibrium chemical reactions, in *AIAA Fluid and Plasma Dynamics Conference* (AIAA, Los Angeles, CA, 1968).

[14] V. T. Baluckram, A. J. Fangman, and D. A. Andrienko, Simulation of oxygen chemical kinetics behind incident and reflected shocks via master equation, J. Thermophys. Heat Transfer **37**, 198 (2023).

[15] J. W. Streicher, A. Krish, and R. K. Hanson, Coupled vibration-dissociation time-histories and rate measurements in shock-heated, nondilute O_2 and O_2-Ar mixtures from 6000 to 14000 K, Phys. Fluids **33**, 056107 (2021).

[16] H. Bethe and E. Teller, Deviations from thermal equilibrium in shock waves, Technical Report X-117 (Aberdeen Proving Ground, MD, 1941).

[17] V. Laporta, K. Heritier, and M. Panesi, Electron-vibration relaxation in oxygen plasmas, Chem. Phys. **472**, 44 (2016).

[18] A. Gnoffo, N. Gupta, and L. Shinn, Conservation equations and physical models for hypersonic air flows in thermal and chemical nonequilibrium, Report Number: 2867, NASA Technical Paper, National Aeronautics and Space Administration (1989).

[19] M. S. Grover, T. E. Schwartzentruber, Z. Varga, and D. G. Truhlar, Vibrational energy transfer and collision-induced dissociation in $O+O_2$ collisions, J. Thermophys. Heat Transfer **33**, 797 (2019).

[20] R. C. Millikan and D. R. White, Systematics of vibrational relaxation, J. Chem. Phys. **39**, 3209 (1963).

[21] K. M. Hanquist and I. D. Boyd, Modeling of electronically excited oxygen in O_2-Ar shock tube studies, in *AIAA Aviation 2019 Forum* (American Institute of Aeronautics and Astronautics, Dallas, TX, 2019).

[22] J. W. Streicher, A. Krish, R. K. Hanson, K. M. Hanquist, R. S. Chaudhry, and I. D. Boyd, Shock-tube measurements of coupled vibration-dissociation time-histories and rate parameters in oxygen and argon mixtures from 5000 K to 10000 K, Phys. Fluids **32**, 076103 (2020).

[23] C. Park, Two-temperature interpretation of dissociation rate data for N_2 and O_2, in *26th Aerospace Sciences Meeting* (American Institute of Aeronautics and Astronautics, Reno, NV, 1988).

[24] M. G. Kapper and J.-L. Cambier, Ionizing shocks in argon. Part I: Collisional-radiative model and steady-state structure, J. Appl. Phys. **109**, 113308 (2011).

[25] J. G. Kim and I. D. Boyd, Master equation analysis of post normal shock waves of nitrogen, J. Thermophys. Heat Transfer **29**, 241 (2015).

[26] S. S. Lazdinis, Free electron and vibrational temperature nonequilibrium in high temperature nitrogen, Phys. Fluids **17**, 1539 (1974).

[27] M. Nishida and M. Matsumotob, Thermochemical nonequilibrium in rapidly expanding flows of high-temperature air, Z. Naturforsch. A **52**, 358 (1997).

[28] O. Zatsarinny, Y. Wang, and K. Bartschat, Electron-impact excitation of argon at intermediate energies, Phys. Rev. A **89**, 022706 (2014).

[29] S. S. Tayal and O. Zatsarinny, B-spline R-matrix-with-pseudostates approach for excitation and ionization of atomic oxygen by electron collisions, Phys. Rev. A **94**, 042707 (2016).

[30] I. Shkarofsky, M. Bachynski, and T. Johnston, Collision frequency associated with high temperature air and scattering cross-sections of the constituents, Planet. Space Sci. **6**, 24 (1961).

[31] J. P. Appleton and K. N. C. Bray, The conservation equations for a non-equilibrium plasma, J. Fluid Mech. **20**, 659 (1964).

[32] C. Park, *Nonequilibrium Hypersonic Aerothermodynamics* (John Wiley & Sons, New York, 1990).

[33] T. T. Aiken, Detailed modeling and sensitivity analysis of nonequilibrium thermochemistry in shock-heated gases, Doctoral thesis, University of Colorado, Boulder, CO, 2023.

[34] A. Bultel, B. van Ootegem, A. Bourdon, and P. Vervisch, Influence of Ar_2^+ in an argon collisional-radiative model, Phys. Rev. E **65**, 046406 (2002).

[35] A. Bourdon, Y. Térésiak, and P. Vervisch, Ionization and recombination rates of atomic oxygen in high-temperature air plasma flows, Phys. Rev. E **57**, 4684 (1998).

[36] A. Bultel, B. G. Chéron, A. Bourdon, O. Motapon, and I. F. Schneider, Collisional-radiative model in air for earth re-entry problems, Phys. Plasmas **13**, 043502 (2006).

[37] M. Panesi, T. Magin, A. Bourdon, A. Bultel, and O. Chazot, Fire II flight experiment analysis by means of a collisional-radiative model, J. Thermophys. Heat Transfer **23**, 236 (2009).

[38] A. Bourdon and P. Vervisch, Three-body recombination rate of atomic nitrogen in low-pressure plasma flows, Phys. Rev. E **54**, 1888 (1996).

[39] C. J. Ciccarino and D. W. Savin, Electron-impact ionization of atomic nitrogen, J. Thermophys. Heat Transfer **33**, 154 (2019).

[40] W. M. Huo, Y. Liu, M. Panesi, A. Wray, and D. F. Carbon, Electron-impact excitation cross sections for modeling non-equilibrium gas, in *53rd AIAA Aerospace Sciences Meeting* (American Institute of Aeronautics and Astronautics, Kissimmee, FL, 2015).

[41] P. Teulet, J. P. Sarrette, and A. M. Gomes, Calculation of electron impact inelastic cross sections and rate coefficients for diatomic molecules. Application to air molecules, J. Quant. Spectrosc. Radiat. Transfer **62**, 549 (1999).

[42] C. Park, Rate parameters for electronic excitation of diatomic molecules 1. Electron-impact processes, in *46th AIAA Aerospace Sciences Meeting and Exhibit* (American Institute of Aeronautics and Astronautics, Reno, NV, 2008).

[43] P. V. Johnson, J. W. McConkey, S. S. Tayal, and I. Kanik, Collisions of electrons with atomic oxygen: Current status, Can. J. Phys. **83**, 589 (2005).

[44] H. Drawin, Atomic cross sections for inelastic electronic collisions, Report Number: EUR-CEA-FC 236, Association Euratom-CEA (Cadarache, France, 1963).

[45] J. Annaloro, A. Bultel, and P. Omaly, Collisional-radiative modeling behind shock waves in nitrogen, J. Thermophys. Heat Transfer **28**, 608 (2014).

[46] D.-H. Kwon and Y.-S. Cho, Electron-impact excitation cross sections for Ar and Ar^+ by unitarized distorted-wave approximation, At. Data Nucl. Data Tables **137**, 101385 (2021).

[47] H. Deutsch, K. Becker, A. Grum-Grzhimailo, K. Bartschat, H. Summers, M. Probst, S. Matt-Leubner, and T. Märk, Calculated cross sections for the electron-impact ionization of excited argon atoms using the DM formalism, Int. J. Mass Spectrom. **233**, 39 (2004).

[48] H. Deutsch, K. Becker, S. Matt, and T. Märk, Theoretical determination of absolute electron-impact ionization cross sections of molecules, Int. J. Mass Spectrom. **197**, 37 (2000).

[49] Y. Sun and A. Dalgarno, Collisional excitation of metastable $O(^1D)$ atoms, J. Chem. Phys. **96**, 5017 (1992).

[50] M. Jamieson, M. Finch, R. Friedman, and A. Dalgarno, Collisional excitation of metastable oxygen $O(^1D)$ atoms through the $B\,^3\Sigma_u^-$ channel of O_2, Planet. Space Sci. **40**, 1719 (1992).

[51] M. A. Blitz, T. J. Dillon, D. E. Heard, M. J. Pilling, and I. D. Trought, Laser induced fluorescence studies of the reactions of $O(^1D_2)$ with N_2, O_2, N_2O, CH_4, H_2, CO_2, Ar, Kr and n-C_4H_{10}, Phys. Chem. Chem. Phys. **6**, 2162 (2004).

[52] M. Capitelli, C. M. Ferreira, B. F. Gordiets, and A. I. Osipov, *Plasma Kinetics in Atmospheric Gases*, Springer Series on Atomic, Optical, and Plasma Physics Vol. 31 (Springer, Berlin, 2000).

[53] R. Atkinson, D. L. Baulch, R. A. Cox, J. N. Crowley, R. F. Hampson, R. G. Hynes, M. E. Jenkin, M. J. Rossi, and J. Troe, Evaluated kinetic and photochemical data for atmospheric chemistry: Part 1—gas phase reactions of O_x, HO_x, NO_x and SO_x species, Atmos. Chem. Phys. Discuss. **3**, 6179 (2003).

[54] A. Lemal, C. M. Jacobs, M.-Y. Perrin, C. O. Laux, P. Tran, and E. Raynaud, Prediction of nonequilibrium air plasma radiation behind a shock wave, J. Thermophys. Heat Transfer **30**, 197 (2016).

[55] D. R. Bates, Theoretical considerations regarding some inelastic atomic collision processes of interest in aeronomy: Deactivation and charge transfer, Planet. Space Sci. **37**, 363 (1989).

[56] K. Schofield, Rate constants for the gaseous interactions of $O(^1D)$ and $O(^1S)$—A critical evaluation, J. Photochem. **9**, 55 (1978).

[57] H. U. Kiefl and J. Fricke, De-excitation of $O(^5S)$ metastables in inelastic collisions with noble gases, J. Phys. B **13**, 1185 (1980).

[58] L. G. Piper, Electronic energy transfer between metastable argon atoms and ground-state oxygen atoms, Chem. Phys. Lett. **28**, 276 (1974).

[59] P. J. Dagdigian, B. E. Forch, and A. W. Miziolek, Collisional transfer between and quenching of the $3p\,^3P$ and ^5P states of the oxygen atom, Chem. Phys. Lett. **148**, 299 (1988).

[60] H. Drawin and F. Emard, Atom-atom excitation and ionization in shock waves of the noble gases, Phys. Lett. A **43**, 333 (1973).

[61] N. Sadeghi, D. W. Setser, A. Francis, U. Czarnetzki, and H. F. Döbele, Quenching rate constants for reactions of $Ar(4p[1/2]^0, 4p[1/2]^0, 4p[3/2]^2$, and $4p[5/2]^2)$ atoms with 22 reagent gases, J. Chem. Phys. **115**, 3144 (2001).

[62] A. V. Volynets, D. V. Lopaev, T. V. Rakhimova, O. V. Proshina, A. A. Chukalovsky, and J. P. Booth, Fast quenching of metastable $O_2(a\,^1\Delta_g)$ and $O_2(b\,^1\Sigma_g^+)$ molecules by $O(^3P)$ atoms at high temperature, Plasma Sources Sci. Technol. **29**, 115020 (2020).

[63] A. P. Billington and P. Borrell, The low-temperature quenching of singlet molecular oxygen $[O_2(a\,^1\Delta_g)]$, J. Chem. Soc., Faraday Trans. 2 **82**, 963 (1986).

[64] C. Yamabe and A. V. Phelps, Excitation of the $O_2(a\,^1\Delta_g)$ state by low energy electrons in O_2-N_2 mixtures, J. Chem. Phys. **78**, 2984 (1983).

[65] M. V. Zagidullin, N. A. Khvatov, I. A. Medvedkov, G. I. Tolstov, A. M. Mebel, M. C. Heaven, and V. N. Azyazov, $O_2(b\,^1\Sigma_g^+)$ Quenching by O_2, CO_2, H_2O, and N_2 at temperatures of 300–800 K, J. Phys. Chem. A **121**, 7343 (2017).

[66] C. Park, Rate parameters for electronic excitation of diatomic molecules II. Heavy particle-impact processes, in *46th AIAA Aerospace Sciences Meeting and Exhibit* (American Institute of Aeronautics and Astronautics, Reno, NV, 2008).

[67] P. M. Borrell, P. Borrell, K. R. Grant, and M. D. Pedley, Rate constants for the energy-pooling and -quenching reactions of singlet molecular oxygen at high temperatures, J. Phys. Chem. **86**, 700 (1982).

[68] P. Borrell, P. M. Borrell, M. D. Pedley, and K. R. Grant, High temperature studies of singlet excited oxygen, $O_2(^1\Sigma_g^+)$ and $O_2(^1\Delta_g)$, with a combined discharge flow/shock tube method, Proc. R. Soc. London A **367**, 395 (1979).

[69] J. Shi and J. R. Barker, Kinetic studies of the deactivation of $O_2(^1\Sigma_g^+)$ and $O(^1D)$, Intl. J. Chem. Kinetics **22**, 1283 (1990).

[70] N. Khvatov, M. Zagidullin, G. Tolstov, I. Medvedkov, A. Mebel, M. Heaven, and V. Azyazov, Product channels of the reactions of $O_2(b\,^1\Sigma_g^+)$, Chem. Phys. **521**, 85 (2019).

[71] R. D. Kenner and E. A. Ogryzlo, Deactivation of $O_2(A\,^3\Sigma_u^+)$ by O_2, O, and Ar, Intl. J. Chem. Kinetics **12**, 501 (1980).

[72] I. A. Kossyi, A. Y. Kostinsky, A. A. Matveyev, and V. P. Silakov, Kinetic scheme of the non-equilibrium discharge in nitrogen-oxygen mixtures, Plasma Sources Sci. Technol. **1**, 207 (1992).

[73] F. An and S. Han, First-principles dynamics of collisional intersystem crossing: Resonance enhanced quenching of $C(^1D)$ by N_2, Phys. Chem. Chem. Phys. **21**, 8645 (2019).

[74] K. M. Hickson, J.-C. Loison, F. Lique, and J. Kłos, An experimental and theoretical investigation of the $C(^1D) + N_2 \rightarrow C(^3P) + N_2$ quenching reaction at low temperature, J. Phys. Chem. A **120**, 2504 (2016).

[75] P. J. Dagdigian, M. H. Alexander, and J. Kłos, Theoretical investigation of the dynamics of $O(^1D \rightarrow {}^3P)$ electronic quenching by collision with Xe, J. Chem. Phys. **143**, 054306 (2015).

[76] Y. Sun and A. Dalgarno, Excitation of two $O(^1D)$ atoms in the collision of ground state oxygen atoms, J. Geophys. Res.: Space Phys. **98**, 13715 (1993).

[77] H. U. Kiefl, W. L. Borst, and J. Fricke, Excitation of $O(^3S)$ resonance radiation in inelastic collisions between $O(^5S)$ metastables and O_2 and N_2 gases, Phys. Rev. A **21**, 518 (1980).

[78] B. A. Cruden and A. M. Brandis, Measurement and prediction of radiative non-equilibrium for air shocks between 7–9 km/s, in *47th AIAA Thermophysics Conference* (AIAA, Denver, CO, 2017), p. 36.

[79] P. O. Haugsjaa and R. C. Amme, Ionization and metastable excitation in low-energy collisions of ground-state argon atoms, J. Chem. Phys. **52**, 4874 (1970).

[80] R. S. Chaudhry, I. D. Boyd, E. Torres, T. E. Schwartzentruber, and G. V. Candler, Implementation of a chemical kinetics model for hypersonic flows in air for high-performance CFD, in *AIAA Scitech 2020 Forum* (American Institute of Aeronautics and Astronautics, Orlando, FL, 2020).

[81] J. G. Kim and I. D. Boyd, Thermochemical nonequilibrium analysis of O_2+Ar based on state-resolved kinetics, Chem. Phys. **446**, 76 (2015).

[82] A. L. Padellec, Partial near threshold cross sections for the associative ionization to form CO^+, NO^+, and O_2^+, Phys. Scr. **71**, 621 (2005).

[83] A. M. Starik, N. S. Titova, and I. V. Arsentiev, Comprehensive analysis of the effect of atomic and molecular metastable state excitation on air plasma composition behind strong shock waves, Plasma Sources Sci. Technol. **19**, 015007 (2010).

[84] P. S. Barklem and R. Collet, Partition functions and equilibrium constants for diatomic molecules and atoms of astrophysical interest, Astron. Astrophys. **588**, A96 (2016).

[85] J. G. Kim, Expansion of the equilibrium constants for the temperature range of 300 K to 20,000 K, Intl. J. Aeronaut. Space Sci. **17**, 455 (2016).

[86] C. Laux, Optical diagnostics and radiative emission of air plasmas, Ph.D. thesis, Stanford University (1993).

[87] A. Kramida, Yu. Ralchenko, J. Reader, and NIST ASD Team, *NIST Atomic Spectra Database* (version 5.11), [Online]. Available: https://physics.nist.gov/asd [Tue Apr 02 2024] (National Institute of Standards and Technology, Gaithersburg, MD, 2023), doi: https://doi.org/10.18434/T4W30F.

[88] T. Holstein, Imprisonment of resonance radiation in gases, Phys. Rev. **72**, 1212 (1947).

[89] T. Holstein, Imprisonment of resonance radiation in gases. II, Phys. Rev. **83**, 1159 (1951).

[90] B. A. Cruden, personal communication (2023).

[91] A. M. Brandis and B. A. Cruden, NEQAIR v15.0 release notes Nonequilibrium and Equilibrium Radiative Transport and Spectra Program (2019), p. 40.

[92] Y. Li, S. Wang, C. L. Strand, and R. K. Hanson, Development of a Stark shift measurement technique using excited-state oxygen atoms to determine electron number density in shock heated O_2-Ar above 10000 K, Plasma Sources Sci. Technol. **30**, 025007 (2021).

[93] K. E. Harwell and R. G. Jahn, Initial ionization rates in shock-heated argon, krypton, and xenon, Phys. Fluids **7**, 214 (1964).

[94] A. J. Kelly, Atom-atom ionization cross sections of the noble gases—Argon, krypton, and xenon, J. Chem. Phys. **45**, 1723 (1966).

[95] H. Wong and D. Bershader, Thermal equilibration behind an ionizing shock, J. Fluid Mech. **26**, 459 (1966).

[96] E. J. Morgan and R. D. Morrison, Ionization rates behind shock waves in argon, Phys. Fluids **8**, 1608 (1965).

[97] I. I. Glass and W. S. Liu, Effects of hydrogen impurities on shock structure and stability in ionizing monatomic gases. Part 1. Argon, J. Fluid Mech. **84**, 55 (1978).

[98] A. Krish, personal communication (2023).

[99] T. I. McLaren and R. Hobson, Initial ionization rates and collision cross sections in shock-heated argon, Phys. Fluids **11**, 2162 (1968).

[100] H. Mirels, Test time in low-pressure shock tubes, Phys. Fluids **6**, 1201 (1963).

[101] Y. Li, personal communication (2023).

[102] M. Panesi, T. E. Magin, A. Bourdon, A. Bultel, and O. Chazot, Electronic excitation of atoms and molecules for the FIRE II flight experiment, J. Thermophys. Heat Transfer **25**, 361 (2011).

[103] T. K. West, C. O. Johnston, and S. Hosder, Uncertainty and sensitivity analysis of afterbody radiative heating predictions for earth entry, J. Thermophys. Heat Transfer **31**, 294 (2017).

[104] T. K. West and S. Hosder, Uncertainty quantification of hypersonic reentry flows with sparse sampling and stochastic expansions, J. Spacecr. Rockets **52**, 120 (2015).

[105] T. K. West, A. J. Brune, S. Hosder, and C. O. Johnston, Uncertainty analysis of radiative heating predictions for Titan entry, J. Thermophys. Heat Transfer **30**, 438 (2016).

[106] G. Deman, K. Konakli, B. Sudret, J. Kerrou, P. Perrochet, and H. Benabderrahmane, Using sparse polynomial chaos expansions for the global sensitivity analysis of groundwater lifetime expectancy in a multi-layered hydrogeological model, Reliab. Eng. Syst. Safety **147**, 156 (2016).

[107] N. Lüthen, S. Marelli, and B. Sudret, Sparse polynomial chaos expansions: Literature survey and benchmark, SIAM/ASA J. Uncertainty Quant. **9**, 593 (2021).

[108] J. Feinberg and H. P. Langtangen, Chaospy: An open source tool for designing methods of uncertainty quantification, J. Comput. Sci. **11**, 46 (2015).

[109] O. Tange, GNU Parallel 20230222 ('Gaziantep') (2023), Zenodo, doi:10.5281/zenodo.7668338.

[110] E. van den Berg and M. P. Friedlander, Probing the Pareto frontier for basis pursuit solutions, SIAM J. Sci. Comput. **31**, 890 (2009).

[111] E. van den Berg and M. P. Friedlander, Sparse optimization with least-squares constraints, SIAM J. Optim. **21**, 1201 (2011).